Czech Technical University in Prague
Faculty of Nuclear Sciences and Physical Engineering

Department of Physical Electronics
Study programme: Physical electronics
Branch of study: Photonics

Nízkoteplotní studium křemíkových vakancí v diamantových tenkých vrstvách

Low-temperature investigations of silicon vacancy centers in diamond thin films

MASTER'S THESIS

Author: Bc. Irena Bydžovská
Supervisor: RNDr. Lukáš Ondič, PhD.
Year: 2022/2023

ČESKÉ VYSOKÉ UČENÍ TECHNICKÉ V PRAZE
FAKULTA JADERNÁ A FYZIKÁLNĚ INŽENÝRSKÁ
Katedra fyzikální elektroniky

ZADÁNÍ DIPLOMOVÉ PRÁCE

Student:	**Bc. Irena B y d ž o v s k á**
Studijní program:	**Fyzikální elektronika**
Specializace:	**Fotonika**
Akademický rok:	**2022/2023**
Název práce: (česky)	**Nízkoteplotní studium křemíkových vakancí v diamantových tenkých vrstvách**
Název práce: (anglicky)	**Low-temperature investigations of silicon vacancy centers in diamond thin films**
Jazyk práce:	**Angličtina**

Cíl práce:

Cílem je porovnat nízkoteplotní fotoluminiscenční charakteristiky křemíkových diamantových center v různých typech diamantových substrátů a pochopit mechanizmus emise světla z center a ostatních defektů diamant.

.

Pokyny pro vypracování:

1. Vypracujte rešerši zabývající se nízkoteplotním měřením optických vlastností barevných center v diamantu.
2. Seznamte se s principy měření v optickém kryostatu.
3. Změřte fotoluminiscenci a doznívání fotoluminiscence vybraného standardního materiálu za nízkých teplot (4 K)
4. Změřte doznívání fotoluminiscence křemíkových optických center a ostatních defektů v různých typech diamantu jakožto funkci teploty vzorku.
5. Vyhodnoťte změřené data ve vhodném programu a výsledky porovnejte s literaturou

Doporučená literatura:

1. Neu E., Fischer M., Gsell S., Schreck M., and Becher C., Fluorescence and polarization spectroscopy of single silicon vacancy centers in heteroepitaxial nanodiamonds on iridium, Phys. Rev. B 84, 205211, 2011.
2. Häußler S., Thiering G., Dietrich A., Waasem N., Teraji T., Isoya J., Iwasaki T., Hatano M., Jelezko F., Gali A., and Kubanek A., Photoluminescence excitation spectroscopy of SiV− and GeV− color center in diamond, New J. Phys. 19, 063036, 2017.
3. Jahnke K. D., Sipahigil A., Binder J. M., Doherty M. W., Metsch M., Rogers L. J., Manson N. B., Lukin M. D., and Jelezko F., Electron–phonon processes of the silicon-vacancy centre in diamond, New J. Phys. 17, 043011. 2015.
4. Neu E., Hepp Ch., Hauschild M., Gsell S., Fischer M., Sternschulte H., Steinmüller-Nethl D., Schreck M., and Becher Ch., Low-temperature investigations of single silicon vacancy colour centres in diamond, New J. Phys. 15, 043005, 2013.

Jméno a pracoviště vedoucího práce:

RNDr. Lukáš Ondič, Ph.D.
Fyzikální ústav AV ČR, v.v.i

Jméno a pracoviště konzultanta:

doc. Dr. Ing. Ivan Richter
Katedra fyzikální elektroniky, Fakulta jaderná a fyzikálně inženýrská ČVUT v Praze

Datum zadání: 17. říjen 2022

Datum odevzdání: 3. květen 2023

Doba platnosti zadání je dva roky od data zadání.

.....

Garant programu

.....

Vedoucí katedry

.....

Děkan

ČESKÉ VYSOKÉ UČENÍ TECHNICKÉ V PRAZE Fakulta jaderná a fyzikálně inženýrská

V Praze dne 17.10.2022

Declaration

I hereby declare that I carried out this work independently, and only with the cited sources, literature and other professional sources.

In Prague on 2.5.2023

.....

Bc. Irena Bydžovská

Acknowledgements

I would like to thank my supervisor RNDr. Lukáš Ondič, PhD. who guided me through this project. Furthermore, I would like to thank my supervisor-specialist Doc. Ing. Ivan Richter, Dr. for his insight. Lastly, I would like to thank my friends and family for their continuous support.

Bc. Irena Bydžovská

Title:

Low-temperature investigations of silicon vacancy centers in diamond thin films

Author: Bc. Irena Bydžovská

Department: Department of Physical Electronics
Study programme: Physical electronics
Branch of study: Photonics
Type of thesis: Master's thesis

Supervisor: RNDr. Lukáš Ondič, PhD.
Institute of Physics of the Czech Academy of Sciences
Supervisor-specialist: doc. Ing. Ivan Richter, Dr.
Department of Physical Electronics, Faculty of Nuclear Sciences and Physical Engineering CTU in Prague

Abstract: Light-emitting negatively-charged silicon vacancy (SiV) centers can be formed at high densities in diamond thin films using the chemical vapor deposition process. Diamond thin films can be relatively cheaply fabricated on a large scale, which might be applicable in photonics or biosensing. However, the practical usage of the films is limited due to their polycrystalline nature causing the strain in the material and also the unwanted background photoluminescence (PL). To suppress the strain and the background PL we investigated the influence of deposition process parameters on the optical properties of diamond thin films grown on SiO_2 substrates. Namely, we systematically increased the amount of CH_4 to H_2 from 2 to 15% and studied how it influences the chemical, structural and PL properties of the grown films. Furthermore, we investigated if the growth of a diamond barrier layer on the SiO_2 prior to the deposition of the SiV rich diamond layer will prevent the contamination of the samples with Si from the substrate. To investigate the structural changes, we employed the tools of Raman spectroscopy, scanning electron microscopy and atomic force microscopy. We found that with increasing the amount of CH_4, the Raman diamond peak values increase towards values typical for monocrystalline diamond, the individual diamond grains forming the polycrystalline diamond films get smaller and the surface roughness value decreases. To investigate the optical properties, we employed the tools of steady-state, time-resolved and low temperature time-resolved micro-photoluminescence spectroscopy. We observed shift of the SiV zero phonon line (ZPL) towards the values measured in the monocrystalline diamond and slight decrease in SiV PL decay times with increasing the amount of CH_4. Lastly, we investigated temperature 10-300 K dependence of the SiV ZPL peak position and width, and the SiV ZPL decay times. We observed blue-shifting of the SiV ZPL peak position, broadening of the SiV ZPL, and shortening of the SiV PL decay times with increasing temperature.

Keywords: low-temperature photoluminescence, photoluminescence decay, Raman spectroscopy, diamond, SiV center

Název práce:

Nízkoteplotní studium křemíkových vakancí v diamantových tenkých vrstvách

Autor: Bc. Irena Bydžovská

Abstrakt: Světlo emitující záporně nabitá centra křemík-vakance (SiV) mohou být vytvořena za vysokých hustot v diamantových tenkých vrstvách pomocí chemické depozice z plynné fáze. Tenké diamantové vrstvy mohou být vyrobeny relativně levně ve velkém měřítku a mají potenciální využití ve fotonice či v biosenzorech. Praktické využití těchto vrstev je však limitováno jejich polykrystalickou sktrukturou, která v materiálu způsobuje pnutí a nežádoucí fotoluminiscenční (PL) pozadí. Ve snaze potlačit pnutí a PL pozadí jsme zkoumali vliv parametrů depozičního procesu na tenké diamantové vrstvy rostlé na SiO_2 substrátech. Konkrétně jsme systematicky zvyšovali podíl CH_4 vůči H_2 z 2 na 15% a studovali, jak CH_4 ovlivňuje chemické, strukturní a PL vlastnosti narostlých vrstev. Dále jsme zkoumali vliv diamantové bariéry, která byla na SiO_2 substrát nadeponována před depozicí vrstvy obsahující SiV centra za účelem předejití kontaminace vzorků atomy Si ze substrátu. Pro studium strukturních změn jsme využili Ramanovu spektroskopii, skenovací elektronovou mikroskopii a mikroskopii atomárních sil. Zjistili jsme že s rostoucí koncentrací CH_4 se diamantové Ramanovo maximum tenkých vrstev posouvá k hodnotě typické pro monokrystalický diamant, jednotlivá diamantová zrna tvořící polykrystalické diamantové vrstvy se zmenšují a drsnost povrchu se snižuje. Pro studium optických vlastností jsme využili časově nerozlišenou, časově rozlišenou a nízkoteplotní časově rozlišenou fotoluminiscenční spektroskopii. Pozorovali jsme posun SiV linie nulového fononu (ZPL) směrem k hodnotám naměřeným v monokrystalickém diamantu a mírné zkrácení času doznívání fotoluminiscence SiV ZPL s rostoucím množstvím CH_4. Nakonec jsme zkoumali teplotní závislost 10-300 K polohy maxima, šířky a času doznívání PL SiV ZPL. Pozorovali jsme modrý posuv a rozšíření SiV ZPL a zkracování času doznívání PL SiV center se zvyšováním teploty.

Klíčová slova: nízkoteplotní fotoluminiscence, doznívání fotoluminiscence, Ramanova spektroskopie, diamant, SiV centrum

Contents

Introduction

Diamond is a crystalline form of the elemental carbon with its atoms arranged in a crystal structure called diamond cubic. Due to the arrangement of atoms in diamond, it has the highest hardness and thermal conductivity of any natural material. Diamond also has many attractive optical properties, one of the most important being the possibility to host light-emitting defects, the so-called color centers.

To this day, more than 500 color centers have been discovered in diamond, [1] one of the most important and most studied being the silicon-vacancy (SiV) center. The SiV center garnered attention due to its excellent optical properties such as a narrow zero phonon line and its ability to be used as a single photon emitter. Due to these properties, SiV centers in diamond have strong potential use for bio-imaging, quantum optics, quantum computing and optical sensing.

Diamonds can be fabricated in laboratory in a single-crystal or poly-crystal form. The polycrystalline diamond is composed of diamond grains with sizes starting from 100 nm or even less for very thin layers. [2] The fabrication process of the polycrystalline diamond is much cheaper and faster than the fabrication of single-crystal diamond, however, the optical quality of the polycrystalline diamond is worse due to the presence of a non-diamond carbon phase (sp^2 phase) in-between the grains, which introduces additional absorption losses and background photoluminescence (PL) signal. Therefore, many attempts have been made to lower the presence of the unwanted defects such as the fabrication parameters optimization, the substrate choice, the usage of post-processing techniques. [3, 4] However, there is still a room for improvement. This work deals with thin diamond layers containing SiV centers deposited on SiO_2 substrates and their optical characterization. All of the samples in this work were grown by plasma enhanced chemical vapor deposition technique using CH_4 gas as a source for carbon atoms and a silane gas (SiH_4) as a source of Si atoms for SiV centers.

One of the main goals of this work is to identify deposition parameters that will lead to samples with the optimized SiV to the background PL emission ratio. To identify deposition parameters most suitable for the growth of thin diamond layers with SiV centers, we systematically increased the amount of CH_4 present in the atmosphere during growth from 2%-15%. We also investigated the influence of a protective diamond barrier layer deposited prior to the growth of the SiV rich layer on the optical properties of the resulting samples. This diamond barrier was grown with the intention to prevent the sample contamination with the Si atoms from the SiO_2 substrate during the deposition. To characterize the structural changes,

we employed the tools of Raman spectroscopy, SEM and AFM and to characterize the optical properties, we employed the tools of steady state, low temperature and time-resolved μ-PL spectroscopy. Lastly, we employed the tools of low temperature time-resolved spectroscopy to obtain insight into temperature dependence of the SiV ZPL peak position and width, and the SiV PL decay times.

This work is organized in the following way. Chapter 1 presents a theoretical introduction to the methods used for optical characterization of the samples, gives a basic information on the color centers in diamond and their fabrication and introduces the SiV center in detail. The first part of Chapter 2 covers the samples investigated in this work, the instruments used to prepare them and the instruments used to investigate their structural and optical properties. First part of Chapter 3 introduces the results obtained by Raman spectroscopy, scanning electron microscopy and atomic probe microscopy explaining the structural changes of the grown samples. Second part of Chapter 3 introduces the results obtained by steady-state, time-resolved and low temperature time-resolved μ-PL spectroscopy showing the optical properties of the grown SiV centers. Finally, in Chapter 4 we summarize the obtained results.

Chapter 1

Theoretical part

In this chapter, we introduce the measurement techniques used to characterize the studied samples and the studied color centers. The first half of this chapter introduces Raman spectroscopy and scanning electron microscopy as means to examine the structural changes of the samples and confocal micro-photoluminescence spectroscopy as a mean to examine the optical properties of the centers. The second part of this chapter introduces diamond as a material suitable for the growth of color centers, the physical properties of the chosen color centers, and the fabrication techniques used to generate color centers in diamond. Finally, we briefly compare properties of polycrystalline and monocrystalline diamond.

1.1 Raman spectroscopy

Raman spectroscopy is based on Raman scattering (or Raman effect), which is an inelastic scattering of photons. The sample is illuminated by a laser beam which interacts with the vibrational states of molecules and the incident photons are scattered. The incident photons can be scattered in following ways.

I. **Elastic scattering.** Elastic scattering is the predominant mode of scattering. When scattered elastically, the photon energies of the scattered photons are conserved.

   1. **Rayleigh scattering.** Rayleigh scattering is the elastic scattering of light or other electromagnetic radiation by particles much smaller than the wavelength of the radiation, approximately up to 1/10 of the wavelength. The intensity of the scattering is described by Rayleigh's law

$$I \approx \frac{1}{\lambda^4}, \tag{1.1}$$

   where λ is the wavelength of the radiation. According to Rayleigh's scattering law, the amount of scattering of the light is inversely proportional to the fourth power of the wavelength. [5, 6]

2. **Mie scattering.** Mie scattering is the elastic scattering of particles larger than the wavelength of the incident radiation. Unlike Rayleigh scattering, Mie scattering is not strongly wavelength dependent. [7]

II. **Inelastic scattering.** When scattered inelastically, the photon energies of the scattered photons are not conserved and some of the energy of the particle is either lost or increased. Inelastic scattering is less probable than elastic scattering, only approximately 1 in 1 million scattered photons in scattered inelastically.

Raman scattering. Raman scattering is an inelastic scattering of photons on optical phonon lattice consisting of Stokes and anti-Stokes scattering.

a) **Stokes scattering.** Stokes scattering is a type of an inelastic scattering of photons, where the scattered photons end up having lower energy and higher wavelength than the incident photons. Stokes scattering is more probable than Anti-Stokes scattering.

b) **Anti-Stokes scattering.** Anti-Stokes scattering is a type of an inelastic scattering of photons, where scattered photons end up having higher energy and lower wavelength than incident photons.

The shift in the photon energy during Raman scattering gives us information about the vibrational states of the sample. Each material has its own vibrational fingerprint, which can be used to identify the material composition of the investigated sample.

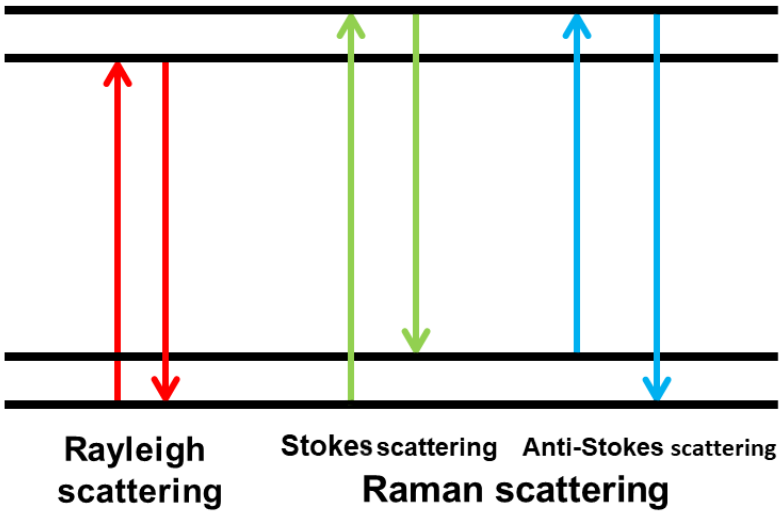

Figure 1.1: Energy-level diagram showing the states involved in elastic Rayleigh and inelastic Raman scattering.

1.2 Scanning electron microscopy

Scanning electron microscopy (SEM) is a type of electron microscopy that employs a focused beam of electrons to scan the surface of a sample. The electrons interact with the surface of the sample in several ways leading to several detection modes. The different types of interactions are shown in Figure 1.2. The most important and used detection modes are secondary electrons and back-scattered electrons.

Secondary electrons. Secondary electrons (SE) are the product of inelastic interaction between the focused electron beam and the sample and originate from the near-surface region of the sample. They also have very low energies in the order of 50 kV, which limits their mean-free path in the sample. The SE detection mode gives us better information about the surface of the sample than the back-scattered electrons.

Back-scattered electrons. Back-scattered electrons (BSE) are the result of elastic interaction between the focused electron beam and the sample. BSE come from deeper situated regions of the sample and provide information about the crystallography of the sample. BSE are highly sensitive to differences in atomic number, where the higher the atomic number is, the brighter the material appears in the obtained image. BSE detection mode is less suitable for surface examination than the SE detection mode.

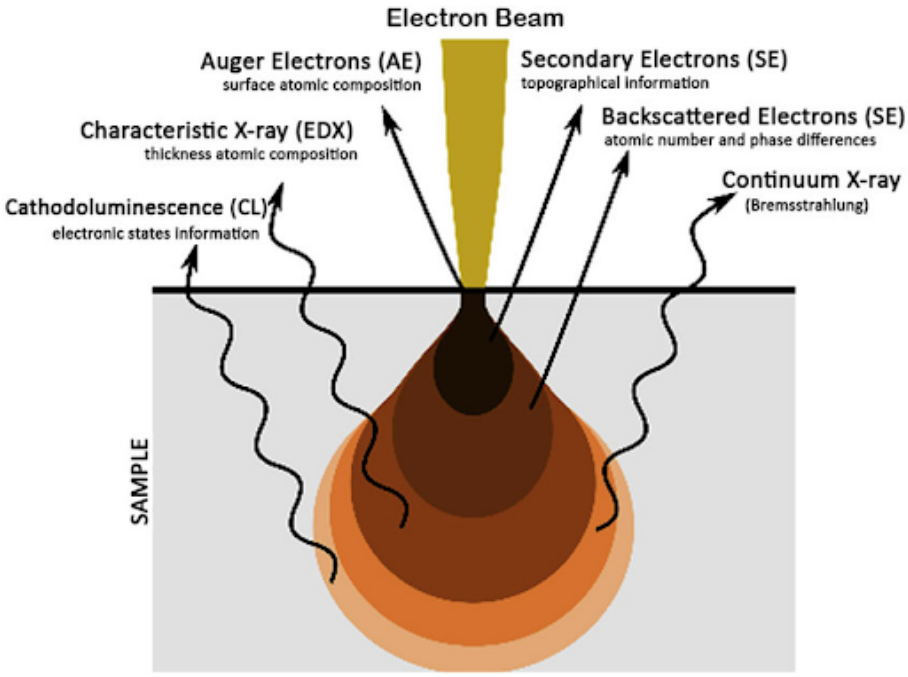

Figure 1.2: Graphical representation of different types of signals produced during SEM measurement. Taken from Thermo Fischer Scientific website. [8]

1.3 Atomic force microscopy

Atomic force microscopy (AFM) is a type of scanning probe microscopy (SPM) that is used for three main purposes - force measurement, topographic imaging, and manipulation. The main advantage of AFM is its ability to obtain images of almost any type of surface, including polymers, ceramics, composites, glass, and biological samples and its demonstrated resolution in the order of nanometers. The AFM consists of a cantilever with a probe in the form of a sharp tip situated at the end of the cantilever. The probe is used to scan the surface of a sample. Depending on the contact of the sharp tip with the surface, we can categorize following imaging modes shown in Figure 1.3.

Contact mode. In the contact mode, the probe is in a constant contact with the surface of the sample. To obtain the signal from the surface, we further use configuration introducing a constant or a feedback parameter, for example the constant force mode or the constant height mode.

Tapping mode. In the tapping mode, the probe oscillates at a high frequency close to the resonance. The frequency and the amplitude of the driving signal are kept constant, leading to a constant amplitude of the probe oscillation as long as there is no interaction with the surface. As the probe gets closer to the surface of the sample, the amplitude of the probe oscillation changes and this change is used to obtain the AFM image. Tapping mode is used mainly for soft samples or liquids.

Non-contact mode. In the non-contact mode, the probe is not in contact with the sample surface but oscillates above it at the resonant or slightly higher frequency. The Van der Waals forces, which are strongest just above the surface, decrease the resonance frequency of the probe. This decrease in the resonant frequency combined with the feedback loop system maintains a constant oscillation frequency by adjusting the tip-to-sample distance in response to the change. Measuring the tip-to-sample distance at each point of the sample allows us to obtain the samples surface topography (AFM images).

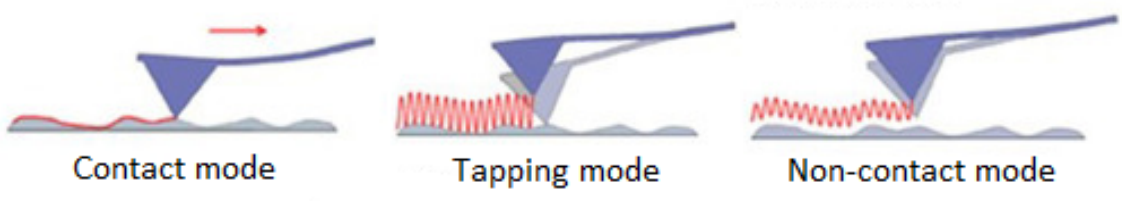

Figure 1.3: Graphical representation of different types of imaging modes used to obtain AFM images. Taken from JPK Instruments handbook and modified. [9]

1.4 μ-photoluminescence spectroscopy

Luminescence is a term describing the process of spontaneous emission of light from a material which is the result of the relaxation of atoms from excited state to the ground state in the material. Photoluminescence (PL) is a special type of luminescence induced by electromagnetic radiation. μ-PL spectroscopy is a technique used to characterize optical properties of a material based on its PL signal which is collected from a small area of the sample ($<$10 μm) employing a microscope objective. In practice, the excitation and the emission light is focused via the similar objective.

1.4.1 Steady-state photoluminescence spectroscopy

Steady-state PL spectroscopy is a type of spectroscopy which uses continuous wave laser to stimulate the emission of photons. We used this measurement technique to obtain the PL of samples as a function of the wavelength.

1.4.2 Time-resolved photoluminescence spectroscopy

Time-resolved PL spectroscopy is a type of spectroscopy which enables to obtain information about the dynamics of the PL signal. It employs pulsed laser to stimulate the emission of photons. The emitted photons can be detected by a number of techniques, such as a photon counting or using the principle of a streak camera.

Photon counting Photon counting is a detection method in which individual photons are counted using a single-photon detector and then converted into the signal. Simple photon counter consists of a photomultiplier, an amplifier, a discriminator, a counter, and a digital-to-analog converter. The number of photons counted by detector N_c is proportional to the number of photons incident on the detector N_i but never equal. In fact, these two values satisfy the following inequation

$$N_c < N_i. \tag{1.2}$$

The proportionality constant between these two values is the quantum efficiency of used photocatode η which describes the quantum yield of the used photocatode. The quantum efficiency of good photomultipliers lies in the range $\eta = 20 - 30\%$. The disadvantage of this detection method is its susceptibility to the detection of unwanted external photons. This problem can be resolved by shielding of instruments, usage of screened cables and good earthing. The tremendous advantage the photon counting method is the ability to detect single photons. [10, 11]

Streak camera A streak camera converts information about time course of luminescence signal into spatial information. The measured light propagates through the spectrometer to the entrance slit and is projected onto the photocatode positioned on the front of the evacuated tube (Figure 1.4). After entering the evacuated tube, the generated electrons are firstly accelerated by the electric field and then deflected by the source of high voltage. As a result, generated electrons are vertically deflected with known velocity and trajectory. This means that time information was successfully converted into spatial information. Generated electrons are subsequently multiplied by the microchannel plate detector and then collected on the phosphor screen. The photons collected on the phosphor screen are then read out by a CCD camera to a computer. In practice, a spectrometer is placed in front of the streak camera detector in order to convert spectral information into the horizontal plane of the CCD camera. The advantage of a streak camera system over the photon counting method is the ability to measure the intensity of the PL as a function of wavelength and time simultaneously. [11]

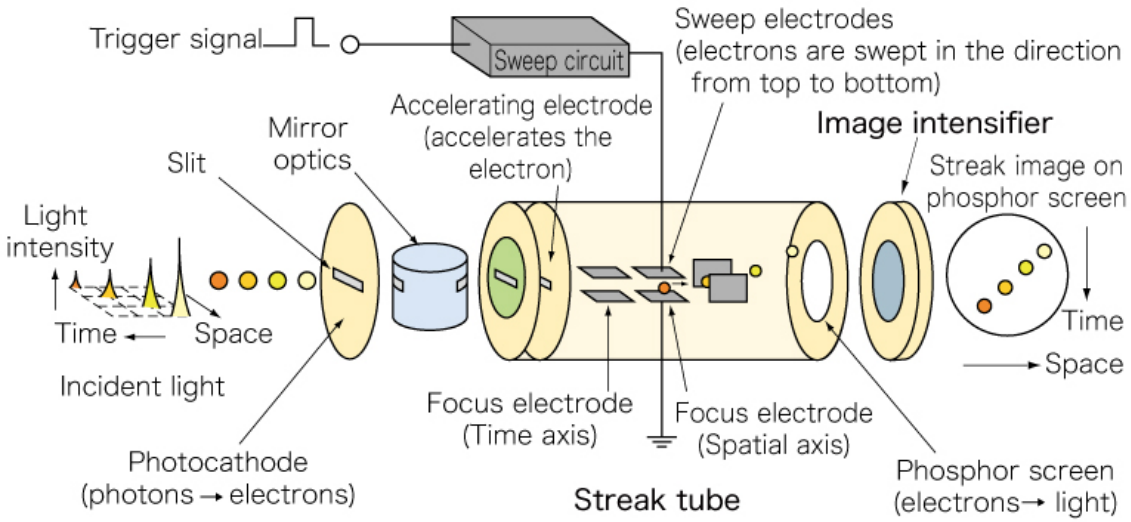

Figure 1.4: The operating principle of the streak camera. Taken from the Hamamatsu Photonics product catalog. [12]

1.4.3 Low temperature time-resolved photoluminescence spectroscopy

Low temperature time-resolved PL spectroscopy uses a pulsed wave laser to stimulate the emission of photons at low temperatures, in our case down to 12 K. We used this measurement technique to obtain temperature dependent PL spectra of a diamond the samples.

1.5 Diamond

Along with graphite, diamond is one of the two main crystalline forms of carbon. In principle, diamond is a metastable phase as graphite is thermodynamically more stable than diamond. Diamond is known to have the highest hardness and thermal conductivity of any natural materials. Along with that, diamond also has excellent optical properties stemming from its crystallographic structure. In this section, we introduce the crystallographic structure and the band structure of diamond.

Crystallographic structure Diamond is a solid form of pure carbon which crystallizes in a crystal structure called diamond cubic. The diamond cubic is a crystal structure which consists of the repeating pattern of a unit cell of 8 atoms. In diamond, each atom of carbon is joined to four neighbouring carbon atoms by sigma (σ) bonds in tetrahedral structure. σ-bonds represent the strongest type of chemical covalent bond and they are formed by overlapping between atomic orbitals. Each bond is at the angle of 109.5° to the adjacent bond. The carbon-carbon bond length is 0.154 nm and the unit cell length is 0.358 nm. [13]

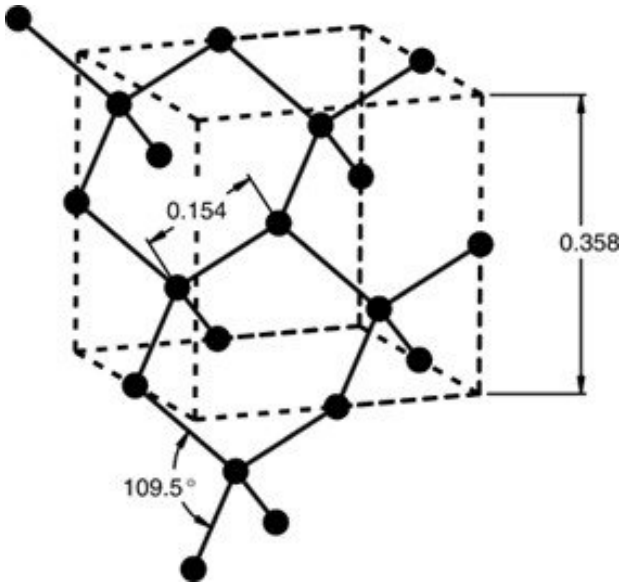

Figure 1.5: The crystallographic structure of diamond. [13]

Band structure of diamond Diamond is a semiconductor with a wide band gap of 5.49 eV corresponding to the deep ultraviolet wavelength of 225 nm. At the Brillouin zone center Γ, the direct gap energy equals 7.3 eV. [1, 14] This means that pure diamond appears as a colorless crystal and does not emit light in the visible nor infrared range. [15] Imperfections in the diamond structure, such as impurity atoms or vacancies, can lead to discrete energy levels within the band gap. Colors in diamond and the visible PL emission then originate from these lattice defects and impurities.

1.6 Color centers in diamond

A color center is a special type of a point crystallographic defect in which a vacancy in a crystal lattice is occupied by one or more unpaired electrons. So far, more then 500 color centers have been discovered in diamond. [1] Color centers have the ability to absorb light and emit photons, and their presence is necessary for obtaining sub-bandgap PL from diamond. The PL emission of a color center is composed of a zero-phonon line (ZPL), which results from a direct transition of the center from an excited to the ground state, and from a phonon-sideband, which originates from the coupling of the excited electrons with the diamond lattice and their subsequent radiative relaxation into the ground state. In this chapter, we introduce the nitrogen-vacancy center and group IV centers, which are among the most studied color centers. The appeal of these particular color centers is their potential to be used in quantum optics, quantum computing and as biosensors.

1.6.1 Nitrogen-vacancy centers

The nitrogen-vacancy (NV) center is a point defect in the diamond lattice that consists of a lattice vacancy and a nitrogen atom, which substitutes for a carbon atom. NV centers form two charge states, neutral NV centers (NV^0) and negative NV centers (NV^-), where NV^- centers have one extra electron located in the vacancy. NV centers, mainly NV^- centers, appeared suitable for applications in quantum technologies, particularly quantum computing and quantum key distribution, due to their capabilities of single photon emission, their long coherence time and the possibility to use them as qubits. [16, 17] ZPL of the NV^0 and NV^- is located at 575 and 638 nm, respectively, as shown in Figure 1.6. However, one of the main disadvantages of NV centers that is preventing their 'real-world' application is the strong coupling of the NV centers with the phonons even at low temperature. Both NV^0 and NV centers have a strong phonon side band (PSB) as shown in Figure 1.6. The ratio between the PL from ZPL and PSB is called the Debye-Waller factor (DWF) and it is typically very low for NV centers. The highest DWF value observed in experiment is 19,3%. [18] Therefore, other types of colors centers with high DWF, such as group IV color centers, are investigated.

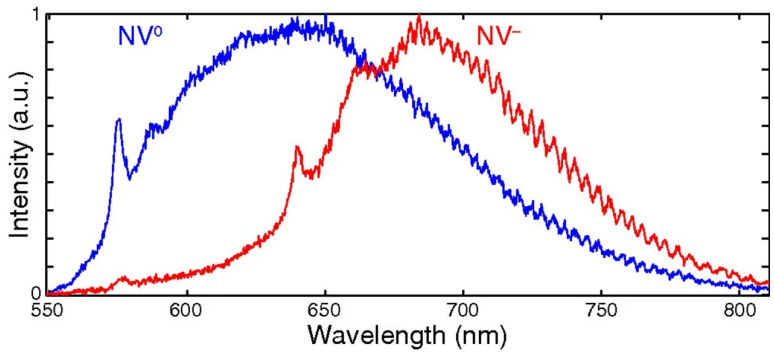

Figure 1.6: PL spectra of NV^0 (blue) and NV^- (red). Taken from [19] and modified.

1.6.2 Group IV color centers

Group IV color centers can be used as single photon emitters with controlled spin. [20] Their potential to be used in quantum optics and quantum computing as qubits is higher than NV centers due to their high DWF (up to 70%). [21, 22] Similarly to the NV centers, the group IV color centers also form neutral and negatively-charged states.

Silicon-vacancy center. The negatively charged silicon-vacancy (SiV^-) center is, following the NV center, the most studied color center in diamond and will be discussed in detail in the following section as it's investigated in this thesis.

Germanium-vacancy center. The germanium vacancy (GeV^-) center is a point defect in the diamond lattice that consists of one germanium atom situated interstitially between two adjacent lattice vacancies. [23] GeV^- ZPL at room temperature is located at 602 nm, as shown in Figure 1.7.

Tin-vacancy center. The tin-vacancy (SnV^-) center is a point defect in the diamond lattice that consists of one tin atom situated interstitially between two adjacent lattice vacancies. SnV^- ZPL at room temperature is located at 620 nm, as shown in Figure 1.7.

Lead-vacancy center. The lead-vacancy (PbV^-) center is a point defect in the diamond lattice that consists of one lead atom situated interstitially between two adjacent lattice vacancies. PbV^- ZPL at room temperature is located at 554 nm, as shown in Figure 1.7.

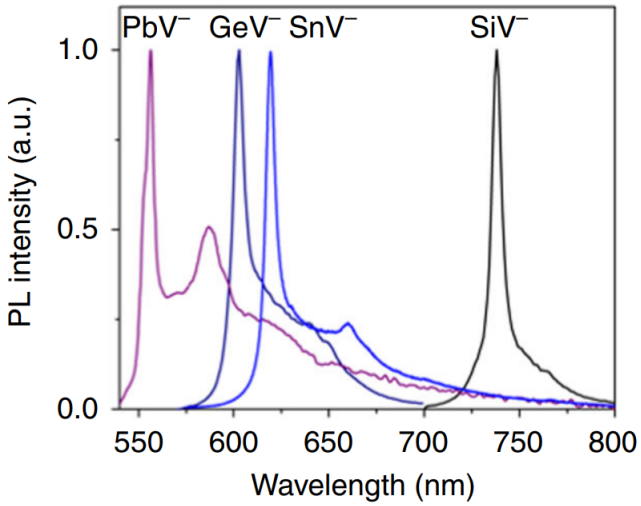

Figure 1.7: Typical PL spectrum of SiV^-, GeV^-, SnV^-, and PbV^- at room temperature. Taken from [20] and modified.

1.7 Silicon-vacancy center in diamond

SiV^- center is one of the most studied group IV color centers due to its excellent optical properties and relatively easy preparation. In this section, we introduce the crystallographic and electronic structure of the SiV^- center and its low temperature optical characteristics.

1.7.1 Crystallographic structure

The SiV^- center is a point defect in the diamond lattice that is formed by replacing two neighboring carbon atoms in the diamond lattice with one silicon atom placed between these two newly formed vacancies. The structure of the SiV^- center is shown in Figure 1.8. This structure has a D_{3d} point group symmetry, meaning that the SiV^- center structure has a 3-fold rotation axis with additional mirror planes parallel to the 3-fold axis, wxhich results in a double orbital degeneracy.

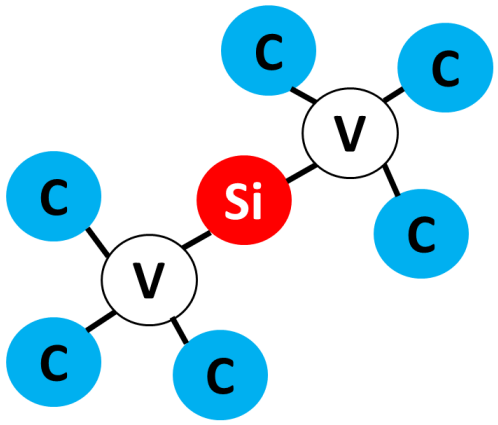

Figure 1.8: Crystallographic structure of the SiV^- center in diamond.

1.7.2 Electronic structure

Due to spin-orbit coupling, both ground and excited states of the SiV^- ZPL are split, resulting in a doublet structure. [24, 25] The doublet structure of the SiV^- center is shown in Figure 1.9. The ground and excited states are therefore split to four energy levels denoted in the bra-ket notation as $|e_1\rangle$, $|e_2\rangle$ and $|g_1\rangle$, $|g_2\rangle$, respectively. At low temperatures (4 K), we can observe four different transitions between these energy states:

$$\begin{aligned} A &: |e_1\rangle \Rightarrow |g_1\rangle\,, \\ B &: |e_1\rangle \Rightarrow |g_2\rangle\,, \\ C &: |e_2\rangle \Rightarrow |g_2\rangle\,, \\ D &: |e_2\rangle \Rightarrow |g_1\rangle\,. \end{aligned} \tag{1.3}$$

Applying strong laser beam, the four energy states can be further splitted. The splitting of energy states under a strong laser beam is called the Autler-Townes effect. The Autler-Townes effect (also known as AC Stark effect) is the dynamical equivalent to the Stark effect, which describes the splitting of energy states under a constant electric field. After applying strong laser beam on the transition D, we obtain four new energy levels: $|e_2, n\rangle$, $|g_1, n+1\rangle$, $|e_2, n-1\rangle$, and $|g_1, n\rangle$. [26] These four energy levels are called dressed states. In quantum optics, dressed states are eigenstates of the total Hamiltonian of the system including interactions. The dynamics of the system is then fully described as the superposition of said dresses states. [27] Each two dressed states created by the Autler-Townes effect are separated by energy given by the following formula

$$\Omega_{AT} = \sqrt{\Delta^2 + \Omega^2}, \tag{1.4}$$

where Δ is the difference between the resonance frequency of the system and the laser's wavelength and Ω is the Rabi frequency, which describes the fluctuations in the population of two level systems. [26, 27] The split of the states $|e_2\rangle$ and $|g_1\rangle$ by the Autler-Townes effect into the doublet states separated by the energy Ω_{AT} results in the creation of symmetrical Mollows triplets which are signature for dressed states. The graphical representation of energy states, possible transitions between energy states and the Autler-Townes effect is shown in Figure 1.9.

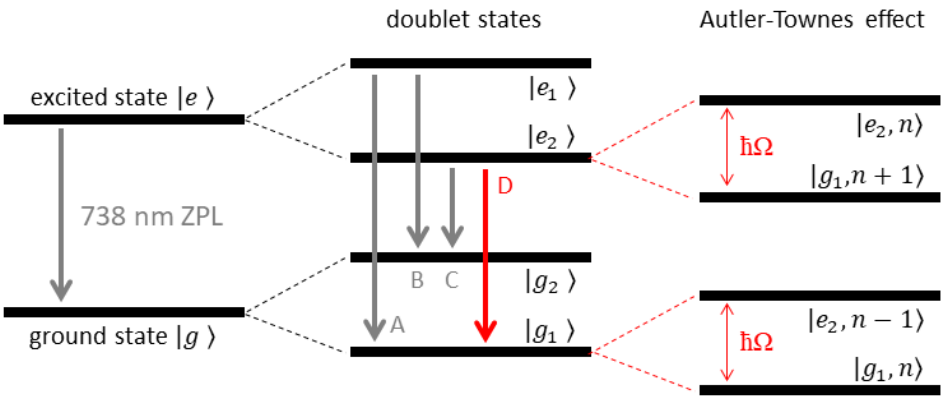

Figure 1.9: Graphical representation of the SiV^- ZPL split and the Autler-Townes effect.

1.7.3 Low temperature optical characteristics

The PL spectra of SiV centers are temperature dependent and decreasing the temperature of the studied material leads to uncovering a four-line structure corresponding to the electronic structure of the SiV center discussed in section 1.7.2. [28] The four-line structure of the SiV ZPL in monocrystalline diamond appearing at low temperatures is shown in Figure 1.10. At room temperature, the phonon-electron interaction increases resulting in a strong broadening of the PL spectra and thus overlapping of bands with close energies. [29] The study of the temperature dependence of PL bands can thus provide information about the process of electron-phonon

interaction and spin coherence, which is crucial for quantum optics and quantum computing. [30, 31]

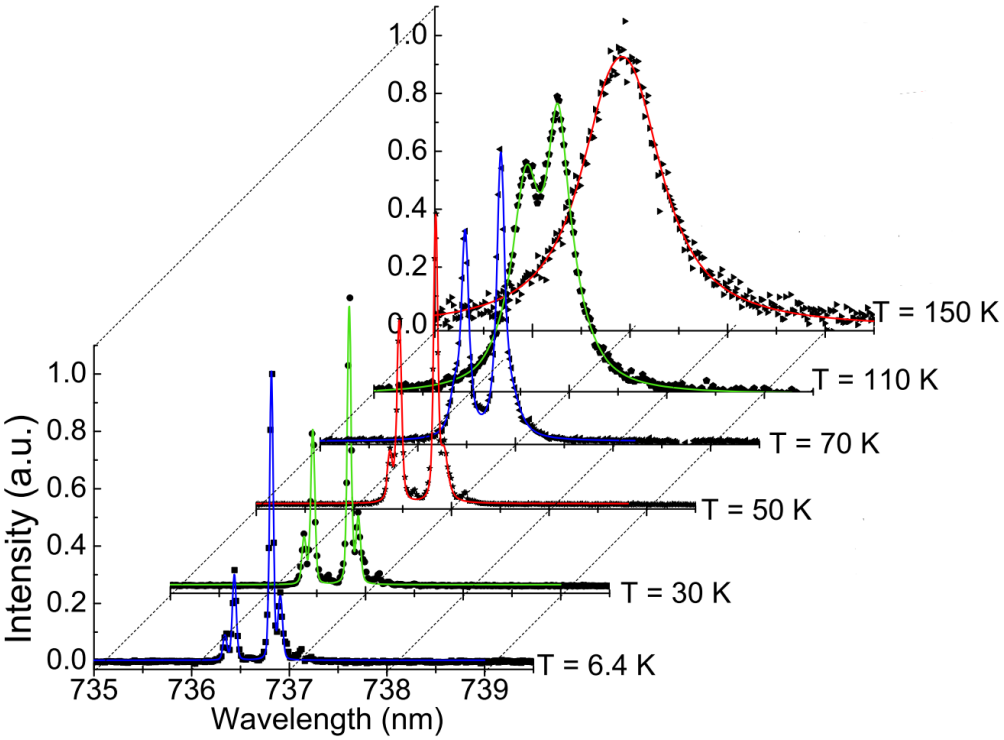

Figure 1.10: Temperature dependence of the SiV ZPL fluorescence in monocrystalline diamond. Taken from [28] and modified.

Furthermore, it has been also observed that upon cooling, the SiV ZPL blueshifts. [28, 29, 32, 33] Blueshifting of the ZPL peak position upon cooling has been also observed for other color centers, e.g. NV centers. [34, 35] For applications in quantum optics, it is necessary to know the precise temperature dependence of SiV ZPL. In literature, the blueshift of SiV ZPL is explained by the contraction of diamond lattice and thus temperature dependent band gap. [36]

1.7.4 Generation of the SiV center in diamond

Polycrystalline and monocrystalline diamond thin films are grown by chemical vapor deposition (CVD). CVD is a vacuum deposition method used mainly to produce solid thin films and coatings. In the typical CVD process, the substrate is exposed to one or more volatile precursors present in the atmosphere. The precursors then react with the substrate on its surface to produce the desired thin layer or coating. The process of deposition of thin diamond films has been studied extensively over the years. [37, 38] SiV centers can be prepared either by ion implantation or CVD followed by the subsequent post-processing in the form of thermal annealing.

Ion implantation Ion implantation is the only method that can generate color centers by implanting impurities after the growth process is complete. These impurities can be implanted at defined positions by masking or ion straggling. Ion straggling is an effect that occurs because of scattering of the incident ions as they travel through the material. The kinetic energy carried by the incident ions will be dissipated as a result of said scattering and the incident ions will change their original direction. The depth of implantation can be thus affected by the kinetic energy of the incident ions because the higher the kinetic energy, the greater the deviation. [4, 20]

Chemical vapor deposition CVD combined with doping can be used to prepare the color centers in-situ. [20] The most common dopants used for SiV center generation are SiH_4 gas and solid source of Si placed in the CVD aparature. The optical properties of the SiV centers, the quality of the grown diamond film, and the deposition process depend on several deposition parameters - temperature, power density and the amount of CH_4 to H_2 used as a precursor. [39] For example, it has been shown that growing the diamond films at low temperatures ($<$400°C) slows down the deposition rate [40, 41] and increasing the power density leads to an improvement in film quality, growth rate, and also to a strong change in film morphology. [39] While influence of CH_4 has been observed, full comparative study is yet to be made.

Thermal annealing Thermal annealing is a post-processing method. In the case of ion implantation, thermal annealing process is needed for achieving the highest possible conversion rate from substitutional atoms into color centers. Thermal annealing causes diffusion of vacancies which is a process where an atom on a normal lattice site jumps into and adjacent vacancy. This process is needed to successfully convert substitutional atoms and vacancies into color centers after ion implantation process. Thermal annealing is also used after the CVD process to repair any additional defects created during the growth. [3, 4]

1.8 Comparison between monocrystalline and polycrystalline diamond layers

The distinction between monocrystalline (MCD) and polycrystalline diamond (PCD) layers lies in their grain structure. MCD (or single crystal) is composed of a single grain of diamond. PCD layers are composed of multiple diamond grains grown close together. This difference in grain structure is cause for several differences between MCD and PCD layers.

Polycrystalline diamond layers. As previously stated, PCD thin films are potentially interesting for applications in sensing. [42] Their surface can be structured into the form of a two-dimensional photonic crystal, [43] which can be further used for the fabrication of two-dimensional photonic crystal-based sensors for biology.

The principle of sensing using photonic crystals is based on the existence of the so-called guided resonances, the resonant wavelength of which strongly depends on the surroundings. [44] Another advantage of PCD is that light-emitting defects, such as color centers discussed in section 1.6, with a defined emission line can be embedded into it during the CVD growth. However, the usage of the emission line of the colour centers, eg. SiV centers, to sense the changes in the surroundings is limited by the presence of defect related background PL stemming from the presence of non-diamond carbon phase, structural defects, and strain in the PCD.

Monocrystalline diamond layers. The single crystal structure of MCD layers opens up new application possibilities. MCD layers are suitable for fabrications of diamond electronic devices due to their high thermal conductivity [45] and high carrier mobility [46]. With PCD layers, both of these parameters depend on the individual diamond grain size. MCD layers are also more suitable for application in quantum optics [47, 48] because unlike PCD layers, they do not posses defect related PL background. The disadvantage of MCD is their costly and time consuming preparation process.

Chapter 2

Experimental part

In this chapter, we will intrdouce the prepared samples, the deposition process and the instruments and measurement setups used to obtain Raman sectra, SEM images, AFM images, steady-state, time-resolved and low temperature time-resolved PL spectra.

2.1 Preparation of samples

To investigate the influence of CH_4 on the grown samples, we prepared group of samples with varying amounts of CH_4 in the atmosphere during growth (2-15%) with and without the diamond barrier. Additionally, we prepared two more samples to test the influence of the diamond barrier and one more sample for the low temperature measurement.

CH_4 series. The samples with varying concentrations of CH_4 were prepared by plasma enhanced chemical vapor deposition (PE CVD) on the Seki Diamond Systems SDS6K (SEKI). SEKI system is designed for long deposition processes of thick diamond layers with the possibility of remote monitoring. The possibility to control the process with a computer ensures stable plasma discharge and allows us to control the density of SiV^- centers by regulating the SiH_4 gas flow. The diamond thin films were grown on SiO_2 substrate (fused silica) with the following deposition parameters: pressure 30 Torr, power 2000 W, temperature 460°C±10°C and gas flow 300 sccm for H_2 and 3 sccm for H_2+SiH_4. These samples were prepared with the following concentrations of CH_4 present in the atmosphere during the growth: 6 sccm (2%), 12 sccm (4%), 18 sccm (6%), 24 sccm (8%), 30 sccm (10%) and 45 sccm (15%). In order to be able to compare the absolute values of the PL intensity, the thickness of the studied samples has been kept similar within the error range. Full list of the samples prepared with varying concentrations of CH_4 is given in the Table 2.1.

Sample	Abbreviation	Thickness [nm]	CH_4
SE221121	SE2%	198	2%
SE221102	SE4%	192	4%
SE221115	SE6%	220	6%
SE221114	SE8%	222	8%
SE221111	SE10%	270	10%
SE221110	SE12%	220	12%
SE221109	SE15%	243	15%

Table 2.1: List of prepared samples including their properties.

CH_4 series with diamond barrier. The samples with varying concentrations of CH_4 and diamond barrier were prepared under the same conditions as the samples without the diamond barrier. The diamond barrier was prepared on the Universal plasmatic system Roth&Rau (RR). RR is a plasmatic system suitable for the growth of nanocrystalline, microcrystalline and porous diamond layers at low pressures and low temperatures. The purpose of this diamond barrier grown on the SiO_2 substrate prior to the deposition of the SiV rich layer is to prevent the contamination of the samples with Si atoms from the substrate. The thickness of the diamond barrier was kept around 100 nm. The samples grown with diamond barrier were discussed in detail in previous work and we will thus include only the most important findings. Full list of the samples prepared with varying concentrations of CH_4 and diamond barrier is given in the Table 2.2.

Sample	Abbreviation	Thickness [nm]	CH_4
SE211214B	SE2%+RR	273	2%
SE210909B	SE4%+RR	297	4%
SE211219	SE6%+RR	280	6%
SE220128	SE8%+RR	256	8%
SE220126	SE10%+RR	270	10%
SE220124	SE15%+RR	263	15%

Table 2.2: List of samples prepared with diamond barrier including their properties.

Barrier control group. To further verify the influence of the diamond barrier, we prepared the samples SEB2% and SEB2%+RR. These samples were prepared with the same concentrations of CH_4 but the sample SEB2% was prepared without the diamond barrier and sample SEB2%+RR was prepared with the diamond barrier. The samples were prepared on the SEKI instrument under the same circumstances as the samples from the CH4% series. The properties of the samples are given in the Table 2.3.

Sample	Abbreviation	Thickness [nm]	CH_4	Diamond barrier
SE211011	SEB2%	220	2%	no
SE211214B	SEB2%+RR	273 + 100	2%	yes

Table 2.3: Properties of the samples SEB2% and SEB2%+RR.

Sample NCD. For the low temperature measurement, we prepared the sample NCD190305A (NCD). The sample NCD was prepared by PE CVD on the Microwave plasmatic system Aixtron (AIXTRON), which is a fully automated system designed to grow diamond layers with the possibility of incorporating color centers. The sample was grown on a SiO_2 substrate with a solid Si source placed near the substrate as a source of Si atoms with the following deposition parameters: pressure 45 Torr, power 3 kW, temperature 750°C and concentration of CH_4 3 sccm (1%). This led to the diamond film with a thickness of 300 nm and a high density of light-emitting negatively charged SiV centers.

Reference diamond (EDP). As a reference to our grown samples, we used the sample EDP. The sample EDP is a monocrystalline diamond with SiV centers that was purchased from EDP Corporation, Japan. Sample EDP was used as a reference due to its properties, such as high quality of SiV centers.

2.2 Measurement methods, setups & instruments

Raman and steady-state micro PL spectroscopy. Raman and steady-state micro PL spectroscopy was measured on the Renishaw inVia Reflex microspectrophotometer using the HeCd laser (Kimmon Dual Wavelength HeCd, model IK5651R-G) with the wavelength of 442 nm for the excitation.

Scanning electron microscopy. SEM images were obtained by MAIA 3 (Tescan) scanning electron microscope in SE mode at 10 kV and with total magnification 60000x.

Atomic force microscopy. AFM measurements were performed on Bruker Dimension ICON AFM in semi-contact PeakForce QNM mode, using conical Aspire CFM probes. Semi-contact PeakForce mode combined with sharp (guaranteed tip radius < 10 nm) probe allows for highly-controlled and accurate low-force measurement. All measurements were processed in Gwyddion software. [49]

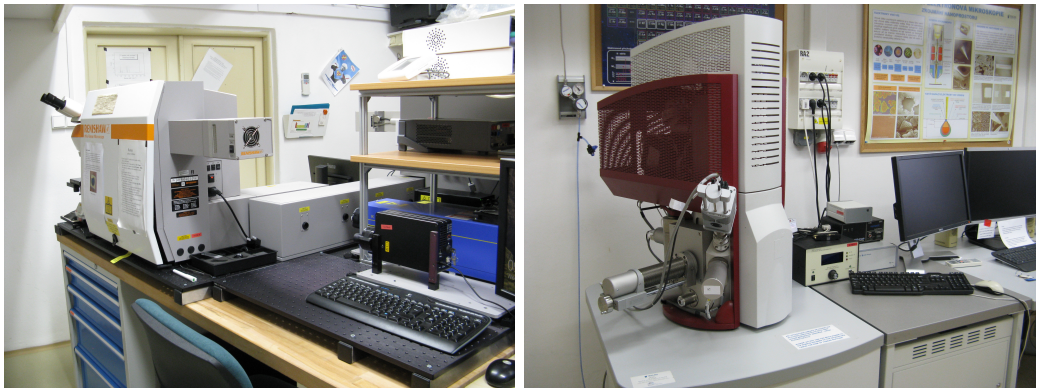

Figure 2.1: Microspectrophotometer Renishaw inVia Reflex (left) and Scanning electron microscope MAIA 3 (right).

Time-resolved PL spectroscopy setup. The source of a laser beam was a solid state Yb:KGW pulsed laser (Pharos, Light Conversion) with the fundamental wavelength of 1030 nm, tunable repetition rate in the range of 1-200 kHz, 200 fs pulses duration, and energies up to 1.5 mJ in the pulse. Second harmonic with the wavelength of 515 nm was generated by inserting a non-linear optical crystal into the path of the laser beam. The laser beam was guided through the set of mirrors and focused on the sample via an objective (NA=0.12). The PL was collected via the similar objective and subsequently focused onto the entrance slit of the spectrometer coupled to the streak camera. Graphical representation of the measurement setup is shown in Figure 2.2.

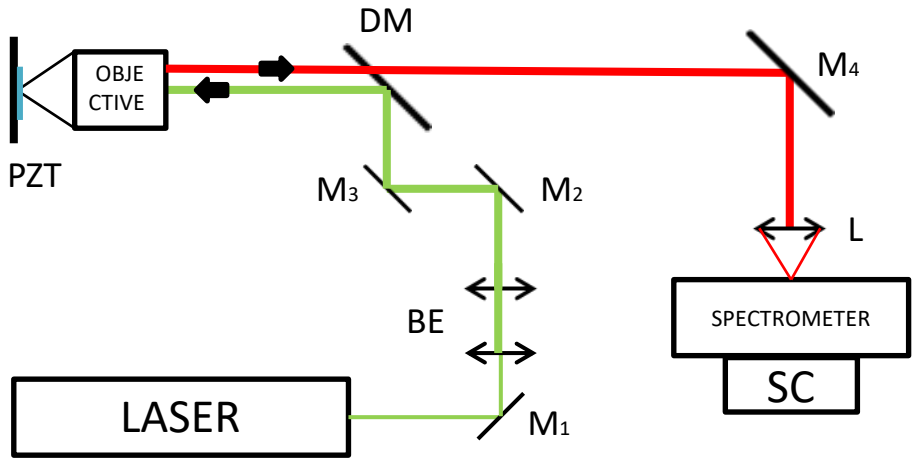

Figure 2.2: Graphical representation of the measurement setup. List of abbreviations: M_{1-4} - mirrors, L - lens, DM - dielectric mirror, BE - beam expander, PZT - piezoelectric table, SC - streak camera.

Low temperature time-resolved PL spectroscopy. Low temperature measurements were performed at FMP CUNI (Faculty of Mathematics and Physics, Charles University, Ke Karlovu 3, 12116 Prague 2) with a measurement setup similar to the one shown in Figrure 2.2 complemented with a He cryostat. The source of a laser beam was a pulsed laser (Tsunami Spitfire, Spectra Physics) followed by a Topas (Light Conversion) tunable optical parametric amplifier providing the excitation wavelength 525 nm, 100 fs pulse duration, and 1 kHz repetition rate. The low temperautre PL decay was measured at the following temperatures: 300 K, 280 K, 260 K, 240 K, 220 K, 200 K, 180 K, 160 K, 140 K, 120 K, 100 K, 80 K, 60 K, 40 K, 20 K and 12 K.

Chapter 3

Results & discussion

In this chapter, we show the results obtained by Raman spectroscopy, SEM, and AFM, which gave us information about the structural changes stemming from increasing the amount of CH_4 in the atmosphere during the growth and from the presence of the diamond barrier. Then we present results of the steady-state, time-resolved, and low temperature time-resolved PL spectroscopy, which provided us with the information about the change in optical properties of the prepared SiV centers.

3.1 Raman spectroscopy

CH_4 series. Raman spectroscopy was measured to obtain information about the structural properties of the samples and the spectral position of the diamond Raman peak, which gives us information about the quality of the prepared sample in comparison with the monocrystalline diamond EDP. Raman spectra of the investigated samples normalized to the diamond peak are shown in Figure 3.1. We can identify the following Raman peakspeaks and bands in the measured spectra of each sample: a diamond peak at 1332 cm^1, a band in the range of 1000-1200 cm^1 corresponding to the trans-polyacetylene (TPA), and a broad band ranging from 1430 to 1650 cm^{-1} which is a superposition of a TPA band (1430-1470 cm^1) and a G-band (1500 to 1650 cm^1). The latter indicates the pres- ence of an amorphous sp^2 carbon situated predominantly in-between the diamond grains, [50, 51, 52] whereas the TPA chains, which are present in the diamond thin films as a by-product of the CVD [53], are placed mainly at the diamond grain boundaries. [54]

Figure 3.2 shows Raman spectra normalized to the diamond peak in the region 1400-1700 cm^{-1} that shows the evolution of TPA and G-band bands with increasing the amount of CH_4 which we will now discuss in detail. First we note that the dip in all the spectra at around 1490 cm^1 is a result of a malfunction in the spectrometer and thus doesn't bear any physical meaning. It was omitted when fitting the spectra. Figure 3.2 a) shows Raman spectra of the samples SE2% and SE4%. We can see that the G-band peaks of these two samples overlap, suggesting very similar amount of sp^2 phase with respect to the diamond phase for both concentrations of CH_4 and a small

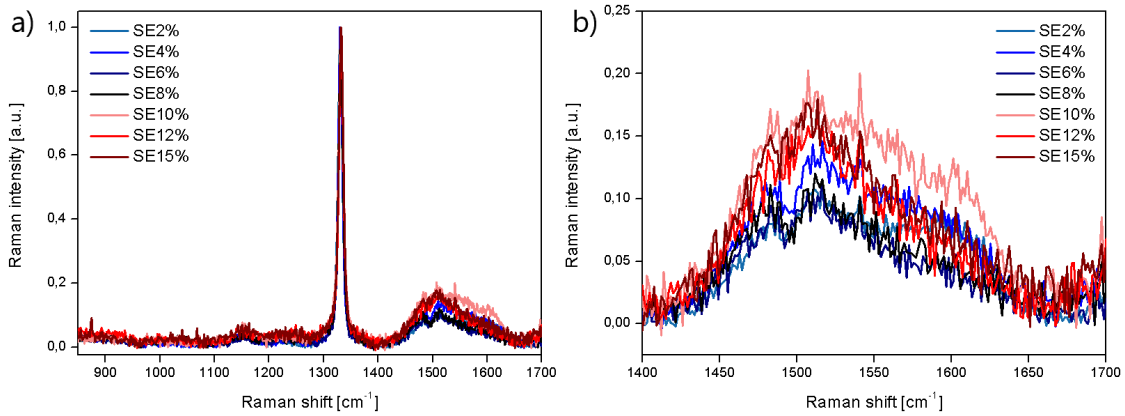

Figure 3.1: a) Raman spectra of the samples SE2-15% normalized to the Raman diamond peak. b) Raman spectra of the samples SE2-15% in the region 1400-1700 cm^{-1}.

increase in the TPA peak intensity for the sample SE4%. Figure 3.2 b) compares Raman spectra of the samples SE4% and SE6%. We see a noticeable decrease in the G-band intensity of the sample SE6% compared to the sample SE4% suggesting decrease in the amount of sp^2 phase with respect to the diamond in this sample. Figure 3.2 c) shows the Raman spectra of the samples SE6% and SE8%. The Raman spetra for these two samples overlap and thus don't show any change. Figure 3.2 d) shows the Raman spectra of the samples SE8% and SE10%. The sample SE10% shows significant rise in he Raman intensity of the non-diamond band compared to the sample SE8% suggesting a rise in the non-diamond phase content compared to the diamond phase for these specific growth parameters. Figure 3.2 e) shows subsequent decrease in the Raman intensity of the non-diamond for the sample SE12%. Finally, Figure 3.2 f) shows shows that increasing the CH_44 content from 12% to 15% do not influence the ratio of diamond and non-diamond phases. From this comparison, we can say that the samples with the lowest amount of sp^2 phase with respect to the diamond phase are the samples SE6% and SE8%. We also observe rise in the TPA peak intensity with increasing the amount of CH_4 which we will be explained in the following two sections.

To obtain the information about the spectral position of the Raman diamond peak, the diamond Raman peak was fitted in Origin [55] with the Lorentz function in the following form

$$y = y_0 + \frac{2A}{\pi}\frac{w}{4(x - x_c)^2 + w^2}, \tag{3.1}$$

where y and x are the independent variables, A is an amplitude, w is the width of fitted peak and x_c is the peak maximum. The obtained spectral positions of Raman diamond peak are shown in Figure 3.3 a) and the detail of the Raman diamond peak of the samples SE2%, SE8%, SE15% and EDP are shown in Figure 3.3 b). For the samples SE2-8%, we see that with increasing the amount of CH_4 in the atmosphere during growth the values of the Raman diamond peak position slowly

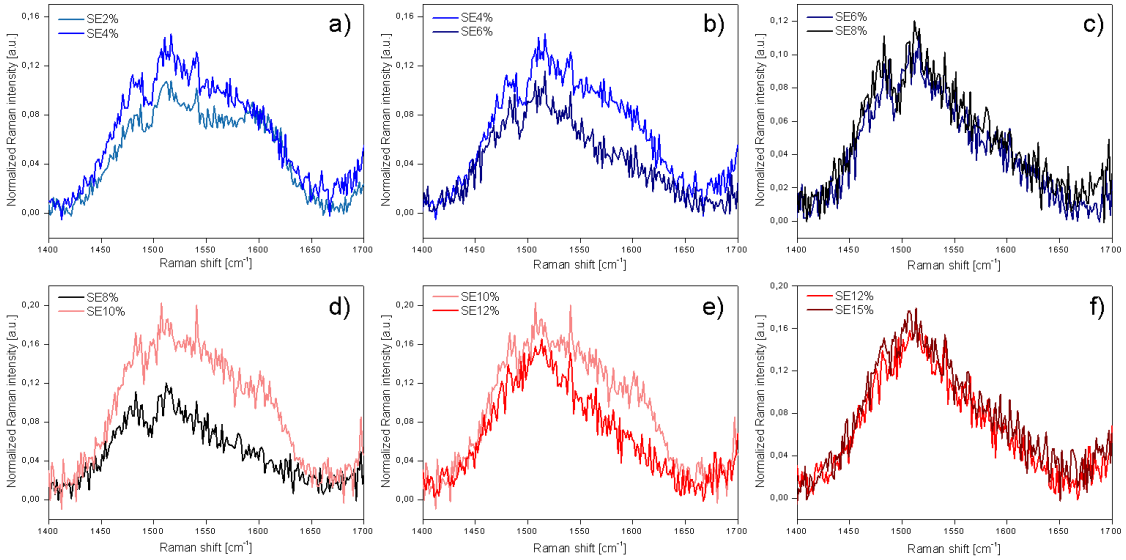

Figure 3.2: Raman spectra normalized to the diamond peak in the region 1400-1700 cm^{-1} of the samples a) SE2-4%, b) SE4-6%, c) SE6-8%, d) SE8-10%, e) 10-12% and f) SE12-15%.

increase towards the monocrystalline reference sample EDP. The samples SE6% and SE8% are the closest to the reference sample EDP in spectral peak position values. For the samples SE10-15%, the spectral peak position values exceed the value of the monocrystalline reference.

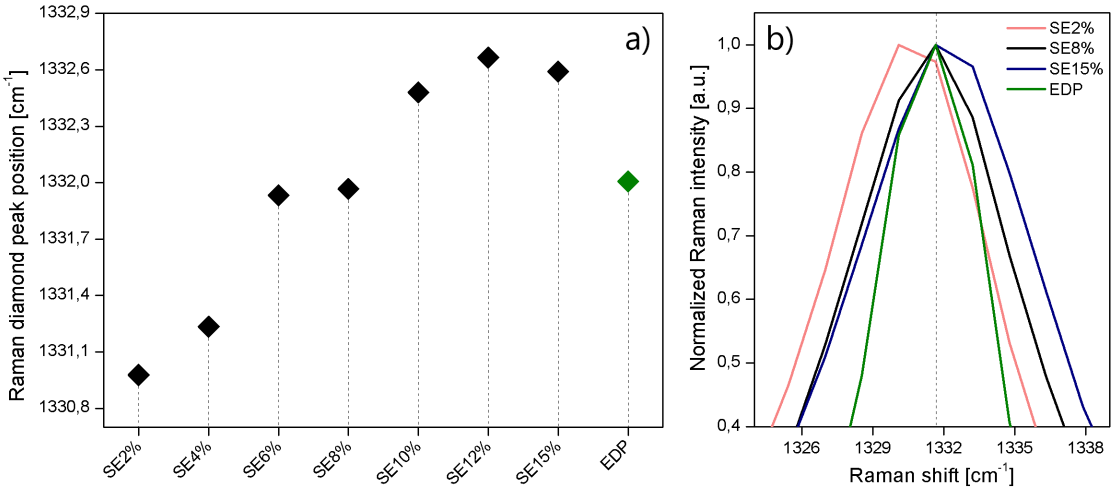

Figure 3.3: a) Raman diamond peak spectral peak position of the samples SE2-15% and EDP obtained by fitting the measured Raman spectra with the Lorentz function 3.1. b) Detail of the Raman diamond peak of the samples SE2%, SE8%. SE15% and EDP.

Furthermore, we fitted the overall the Raman spectra in Python to evaluate the diamond quality factor fq. The quality factor fq reflects the ratio of diamond and non-diamond sp^2 carbon phase. [56, 57] Ideal monocrystalline diamond sample would have fq value of 100%. We calculated the fq factor for individual samples in Python using the following formula

$$fq = \frac{75 \cdot A_{sp^3}}{(75 \cdot A_{sp^3} + A_{non-sp^3})} \cdot 100, \tag{3.2}$$

where A_{sp^3} is the area under the Raman diamond peak and A_{non-sp^3} is the area under the non-diamond Raman phases band composed of the TPA and G-bands. [56] Calculated fq factors of the prepared samples are shown in Figure 3.4 a). We can see that the values of the fq factor is the highest for the sample SE2% and then decreases with increasing the amount of CH_4 used during deposition. We also calculated the the ratios sp^3/TPA and sp^3/G-band shown in Figure 3.4 b). Again, the sample SE2% has the highest sp^3/TPA and sp^3/G-band ratios from the prepared series of samples pointing to the highest intensity of the Raman diamond peak with respect to the non-diamond phases from the prepared series. In Figure 3.4 b) we can also see an increase in the amount of TPA with increasing the amount of CH_4 that will be explained in the two following sections. We would like to note that these results are not consistent with the discussion provided above with respect to the Figure 3.2 which will be investigated in detail in the near future.

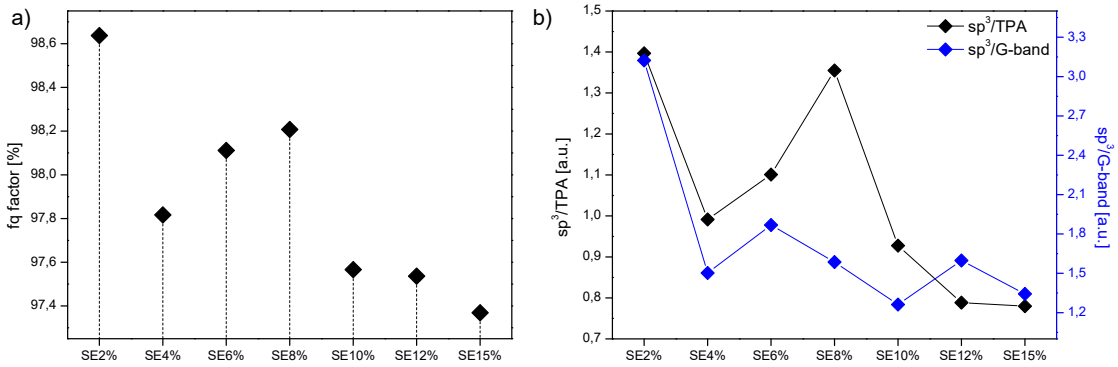

Figure 3.4: a) fq factors and b) sp^3/TPA and sp^3/G-band ratios of the measured samples obtained by fitting the data in Python.

In conclusion, the Raman spectroscopy showed that increasing the amount of CH_4 in the atmosphere during growth leads to shifting the spectral position of the Raman diamond peak of the fabricated polycrystalline diamond. We found that the samples with the most suitable properties for our desired applications are the samples SE6% and SE8% because their Raman diamond peak is at the same spectral position as the monocrystalline diamond reference showing that no-additional stress is present in the samples and except for the sample SE2%, they provide the highest content of the diamond material with respect to the sp^2-related carbon phase.

CH_4 series with diamond barrier. Figure 3.5 shows Raman spectra normalized to the Raman diamond peak of the samples prepared with protective diamond barrier. The spectra shows prominent TPA peak (1500 cm^{-1}) and G-band (1600 cm^{-1}). We can also see that the G-band noticeably increases in intensity for the samples SE8-15% suggesting a higher amount of sp^2 to the diamond phase present in samples deposited with higher concentrations of CH_4. Furthermore, the Raman spectra show a D-band at 1345 cm^{-1} indicating further presence of non-diamond sp^2 carbon phase. [50]

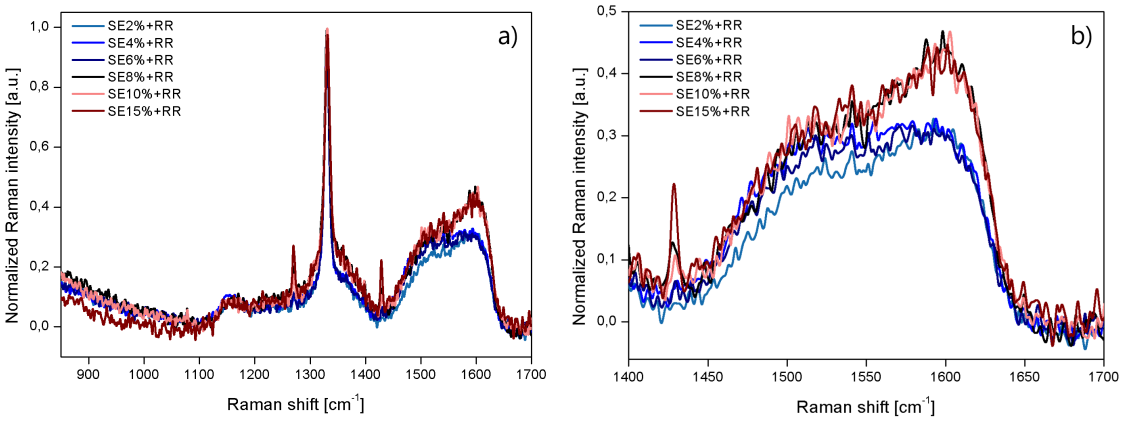

Figure 3.5: a) Raman spectra of the samples SE2-15%+RR normalized to the diamond peak. b) Raman spectra of the samples SE2-15%+RR in the region 1400-1700 cm^{-1}.

The measured diamond Raman peaks of the samples prepared with the diamond barrier were fitted in Origin with the Lorentz function 3.1. The obtained spectral positions of Raman diamond peak are shown in Figure 3.6. We can see that with increasing the amount of CH_4 in the atmosphere during growth, the values of Raman diamond peak slowly increase towards the monocrystalline reference sample EDP meaning that with increasing the amount of CH_4 in the atmosphere, the quality of the fabricated polycrystalline diamond is improving towards the monocrystalline diamond. Unlike the samples prepared without the diamond barrier, the Raman diamond peak values do not reach the monocrystalline diamond value.

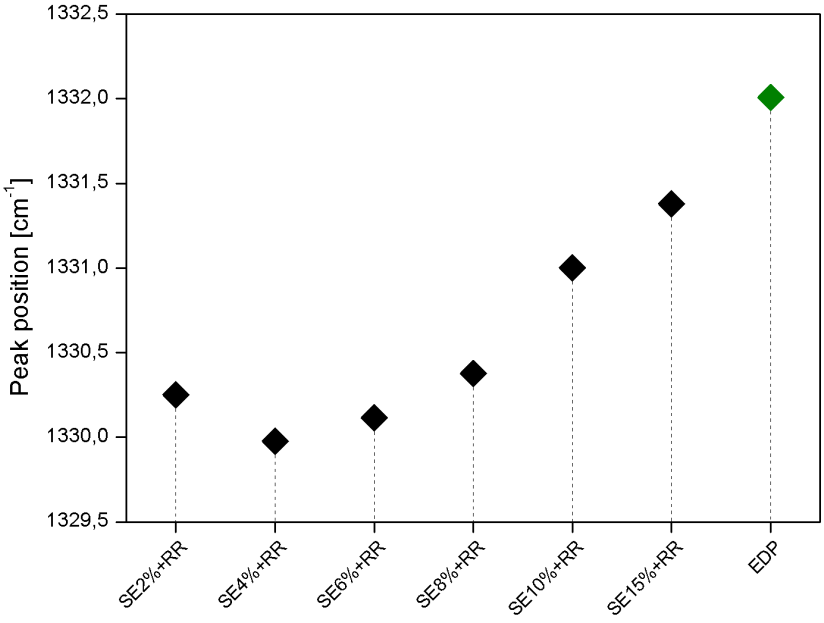

Figure 3.6: Raman diamond peak spectral peak position of the samples SE2-15%+RR and EDP obtained by fitting the measured Raman spectra with the Lorentz function 3.1.

Barrier control group. Figure 3.7 shows the normalized Raman spectra of the samples SEB2% and SEB2%+RR. Confirming the findings from the CH_4 series prepared with and without the diamond barrier, we can see that the presence of diamond barrier causes higher content of non-diamond sp^2 phase in the grown samples as evidenced by the higher G-band intensity and by the occurence of the D-band in the Raman spectrum.

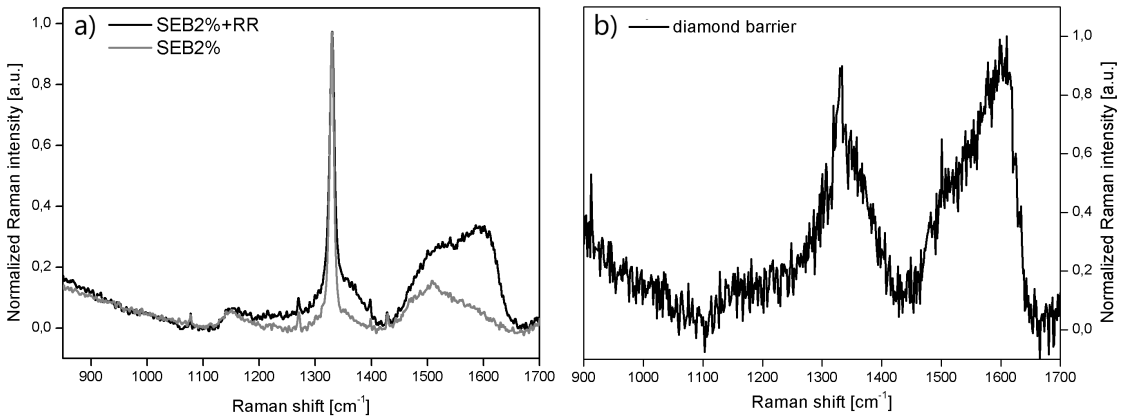

Figure 3.7: a) Raman spectra of the samples SEB2% and SEB2%+RR normalized to the Raman diamond peak. b) Raman spectra of the protective diamond barrier normalized to the G-band.

3.2 Scanning electron microscopy

Polycrystalline diamond films are composed of multiple diamond grains grown closely together. It has been shown that increasing the amount of CH_4 in the atmosphere during the growth of the thin polycrystalline diamond films has an effects on the shape, size and distribution of the individual diamond grains. [57, 58] SEM images of the samples SE2%, SE8%, SE15%, SE2%+RR, SE8%+RR, and SE15%+RR are shown in Figure 3.8. We can see that the samples with the lower concentrations of CH_4 (SE2% and SE2%+RR) are composed of larger diamond grains situated further apart from each other. Increasing the amount of CH_4 present in the atmosphere during growth leads to smaller diamond grain sizes. The individual diamond grains also appear to be situated closer to each other. This can be explained by the smaller diamond grain sizes which would lead to increase in the amount of TPA present on the surface of the individual diamond grains. This corresponds with the Raman spectra discussed in the section 3.1, where we can clearly see an increase in the amount of TPA with increasing the amount of CH_4. In order to quantify differences in between the SEM images of the samples with and without the barrier, further studies are required. However at first sight, the samples grown with the diamond barrier seem to have larger voids in between the grains also for the high CH_4 concentration. The Raman spectra showed increase in the sp^2 to diamond phase ratio which suggest that the voids are filled with the non-diamond sp^2 carbon

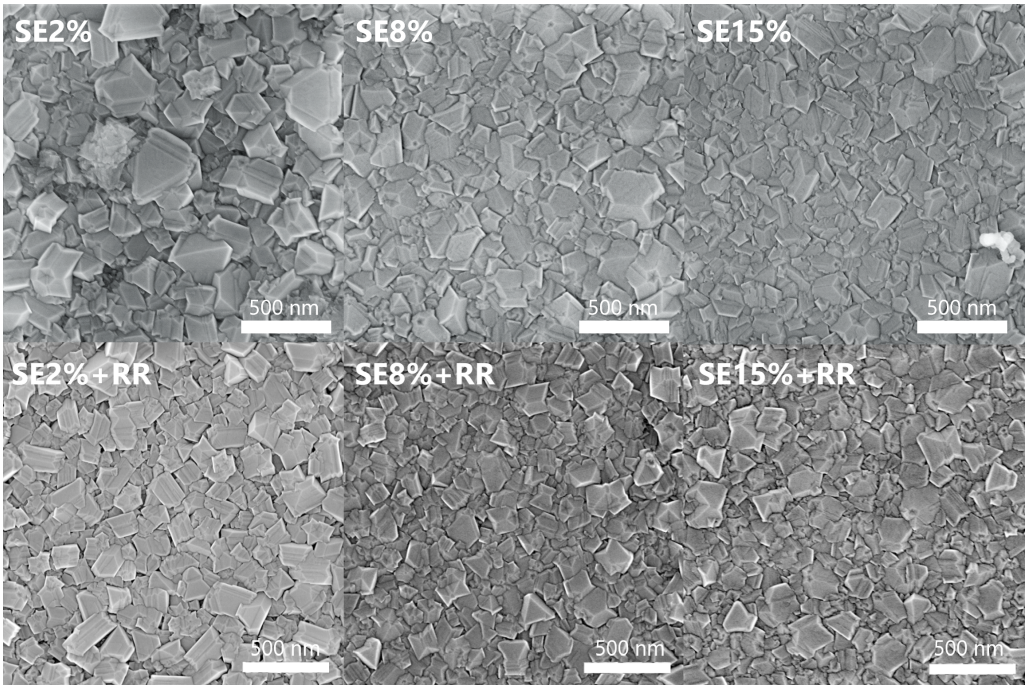

Figure 3.8: SEM images of the samples SE2%, SE8%, SE15%, SE2%+RR, SE8%+RR, and SE15%+RR.

3.3 Atomic force microscopy

AFM images of the samples SE2%, SE8% and SE15% were obtained to calculate the roughness of the surface and to confirm the findings of SEM and Raman. The obtained AFM images are shown in Figure 3.9. The mean square roughness (RMS) of height irregularities was calculated in Gwyddion [49] after filtering the data and getting rid of contamination based irregularities. We obtained the following values of RMS: 41.7 nm (SE2%), 22.4 nm (SE8%) and 16.8 nm (SE15%). We can see that with increasing the amount of the CH_4 in the atmosphere during growth, the RMS value is decreasing, suggesting that the surface of the samples is closing in. This corresponds with the SEM images shown in Figure 3.8 and Raman spectra shown in Figure 3.1 that shows increase in the amount of TPA situated on the surface of grains.

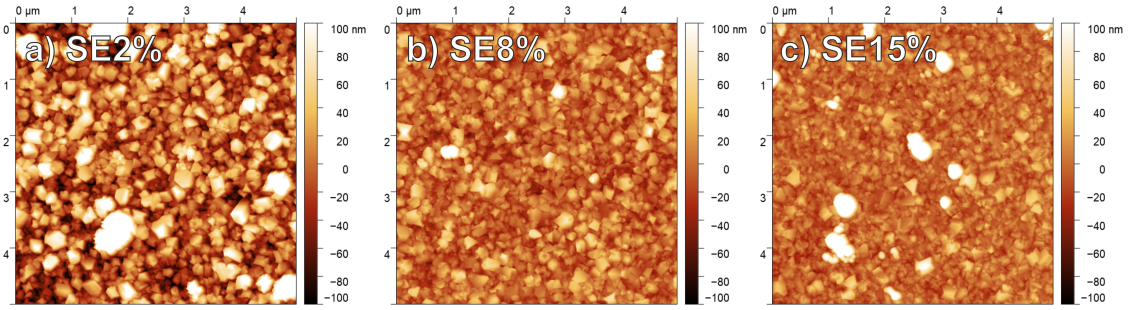

Figure 3.9: AFM images of the samples a) SE2%, b) SE8%, and c) SE15%.

3.4 Steady-state photoluminescence spectroscopy

CH_4 series. Steady-state PL spectroscopy was measured to obtain the information about the SiV ZPL to PL background ratio and the spectral position of the SiV ZPL peak, which gives us information about the quality of the prepared samples in comparison with the monocrystalline diamond EDP. Figure 3.10 shows PL spectra of all the measured samples SE2-15% normalized to the SiV ZPL. The PL spectrum of each sample possesses a clear SiV^- ZPL located at around 739 nm and an adjacent PSB. The SiV ZPL is superimposed on the spectrally broad defect-related PL band ranging from 450-900 nm, which acts as a PL background. We can see that the samples with the lowest intensity of the defect-related PL background with respect to the ZPLintensity are the samples SE4% and SE8%.

To obtain the information about the spectral position of the SiV ZPL, the measured ZPL was fitted in Origin with the Lorentz function 3.1. ZPL peak positions of the measured samples are shown in Figure 3.11 a) and Figure 3.11 b) shows detail of the SiV ZPL of the samples SE2%, SE8%, SE15% and EDP. We can see that with increasing the amount of CH_4 present in the atmosphere during growth, the values of SiV ZPL spectral position slowly decreases towards the monocrystalline reference

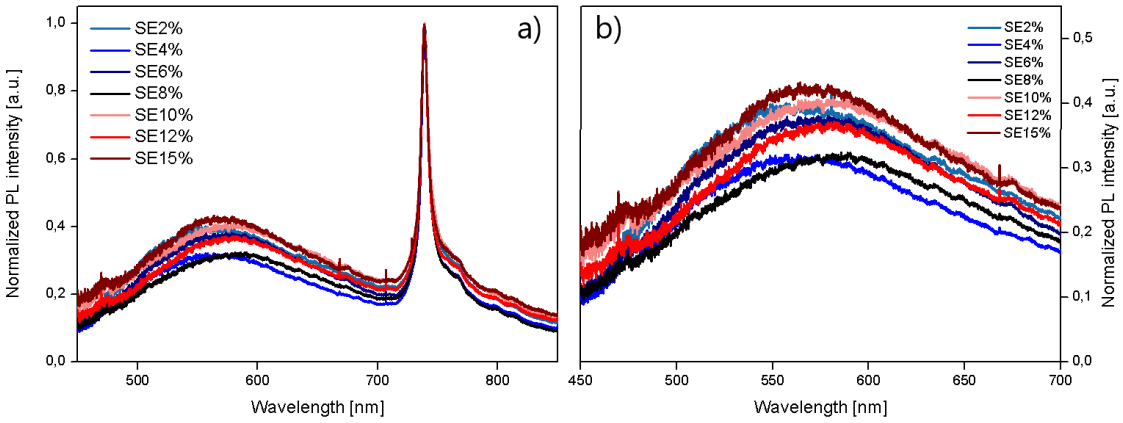

Figure 3.10: a) PL spectra of the samples SE2-15% normalized to the SiV ZPL. b) PL spectra of the samples SE2-15% in the region 450-700 nm showing the defect related PL background.

sample EDP, which shows that with increasing the amount of CH_4 present in the atmosphere during growth the quality of the SiV centers and their optical properties are improving towards the monocrystalline diamond.

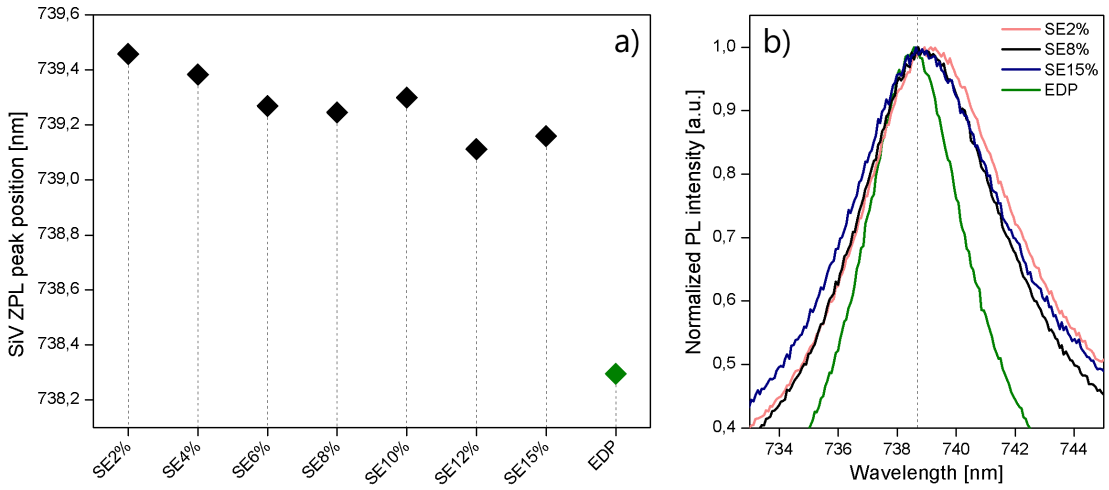

Figure 3.11: a) SiV ZPL spectral peak position of the samples SE2-15% and EDP obtained by fitting the measured PL spectra with the Lorentz function 3.1. b) Detail of the SiV ZPL peak of the samples SE2%, SE8%, SE15%, and EDP.

We further processed the PL spectra in Matlab to obtain the information about the ratio between the SiV emission (ZPL+PSB) and the defect-related PL background. The PL spectra were fitted using Gaussian (g) and Lorentzian (l) functions in the

following form

$$g = \frac{A}{w\sqrt{2\pi}} \cdot \exp\left(\frac{-(x-x_c)^2}{2w^2}\right),$$
$$l = \frac{1}{\pi w} \cdot \frac{w^2}{(x-x_c)^2 + w^2}, \tag{3.3}$$

where x is the independent variable, A is the amplitude, w is the width of fitted peak and x_c is the peak maximum. The PL spectra were fitted in the following way: ZPL at around 738 nm was fitted with a Lorentzian function, PSB at around 770 nm with a Gaussian function, and the PL background ranging from 450-900 nm was fitted with 2 Gaussians. The fit of the PL spectra of the sample SE2% taken as an example is shown in Figure 3.12.

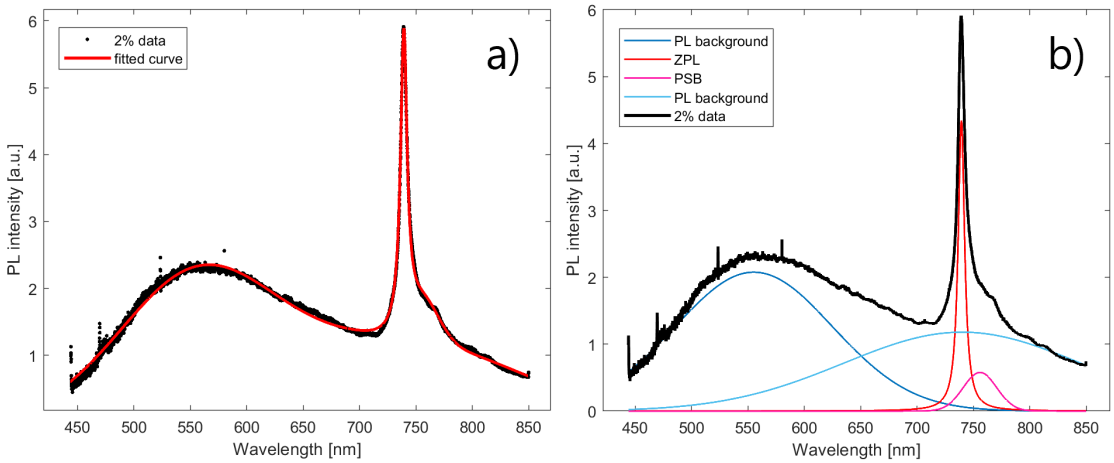

Figure 3.12: Fit of the PL spectrum of the sample SE2% in Matlab. a) Complete fit. b) Fits of individual sections of the PL spectra by Gaussian and Loretzian functions 3.3.

This complex fit of the PL spectra was used to obtain the numerical values of the SiV emission to the defect-related PL background ratio $R_{SiV/bg}$. We calculated the $R_{SiV/bg}$ in Matlab using the formula

$$R_{SiV/bg} = \frac{A_{ZPL} + A_{PSB}}{A_B}, \tag{3.4}$$

where A_{ZPL} is the area under the ZPL peak, A_{PSB} is the area under the PSB peak and A_{bg} is the area under the two Gaussian functions used to fit the PL background for the region 700-800 nm. The calculated values of $R_{SiV/bg}$ are shown in Figure 3.13 a). The samples with the highest values of $R_{SiV/bg}$ are the samples SE4-8%. We further used the results of the fit to calculate the DWF. As previously discussed in Section 1.6.1, the DWF is defined as the ZPL to the PSB ratio. It is known from the literature that the DWF of SiV centers reaches values up to 70%. [21, 22] We calculated the DWF using the following formula

$$DWF = \frac{A_{ZPL}}{A_{ZPL} + A_{PSB}}, \tag{3.5}$$

where A_{ZPL} is the area under the ZPL peak, A_{PSB} is the area under the PSB peak. The calculated values are shown in Figure 3.13 b). All of the calculated DWF values are between 64-69% which is in accordance with literature. [21, 22] We can see that with increasing the amount of CH_4 in the atmosphere during growth, the DWF value decreases, suggesting decrease in the SiV ZPL intensity with respect to the PSB due to the enhanced coupling of centers to phonons or with non-radiative channels.

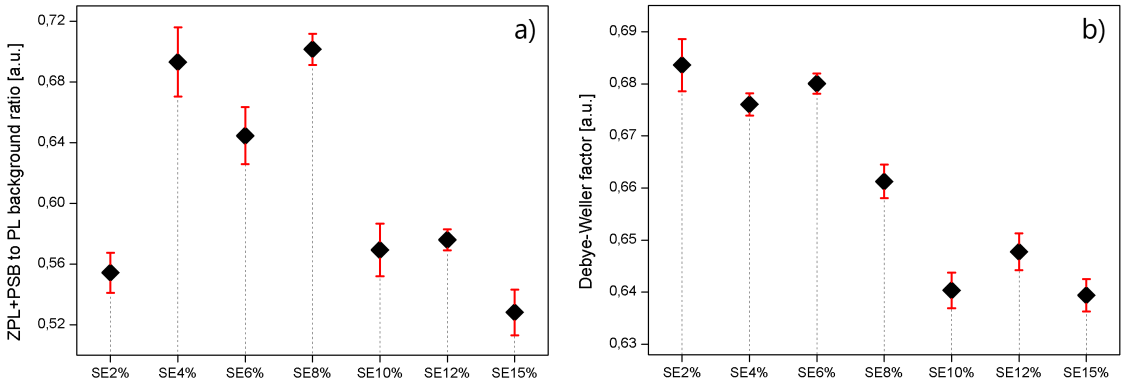

Figure 3.13: Calculated values of a) $R_{SiV/bg}$ and b) DWF.

CH_4 series with diamond barrier. Figure 3.14 shows PL spectra of the samples prepared with diamond barrier normalized to the SiV ZPL. All of the spectra shows defect-related PL background that is very high in intensity. Similarly to the PL spectra of the samples grown without the diamond barrier, the sample with the highest SiV to the PL background ratio is the sample SE4%+RR.

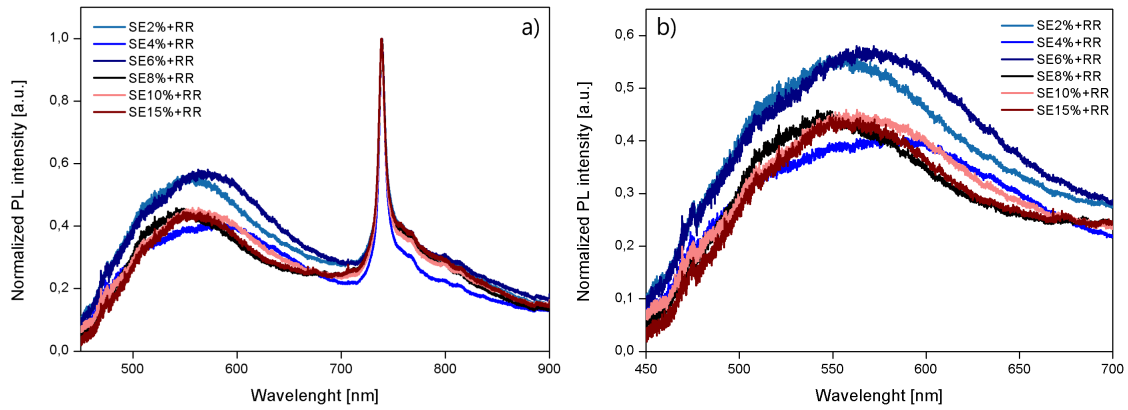

Figure 3.14: a) PL spectra of the samples SE2-15%+RR normalized to the SiV ZPL. b) PL spectra of the samples SE2-15%+RR in the region 450-700 nm showing the defect-related PL background.

To obtain the information about the spectral position of the SiV ZPL, the measured PL spectra of the samples prepared with diamond barrier were fitted in Origin with the Lorentz function 3.1. Peak positions of the measured samples are shown

in Figure 3.15. We can see that with increasing the amount of CH_4 present in the atmosphere during growth, the values of the SiV ZPL spectral position slowly decreases towards the monocrystalline reference sample EDP, which shows that with increasing the amount of CH_4 the quality of the fabricated polycrystalline diamond is improving towards the monocrystalline diamond.

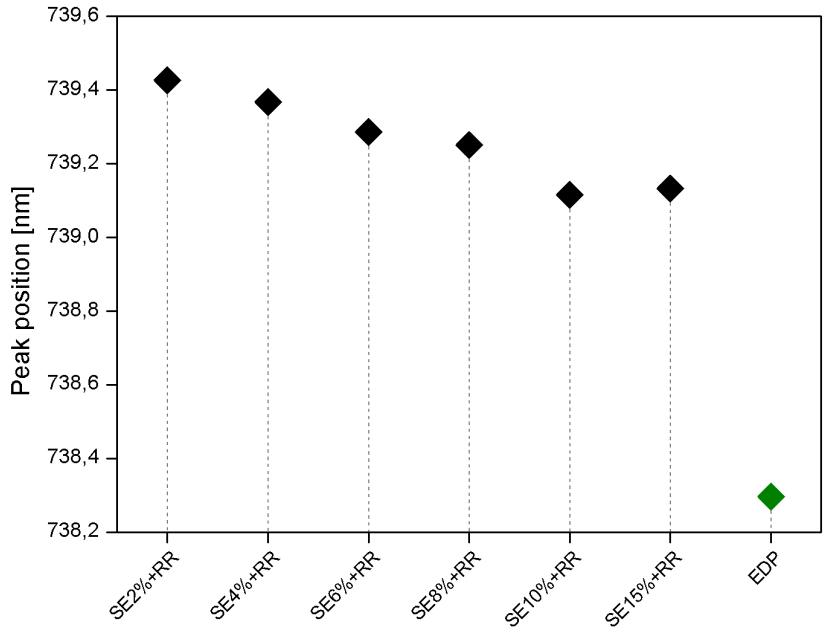

Figure 3.15: SiV ZPL spectral peak position of the samples SE2-15%+RR obtained by fitting the measured PL spectra with the Lorentz function 3.1.

Barrier control group. Figure 3.16 shows normalized PL spectra of the samples SEB2% and SEB2%+RR. We can see that in accordance with the PL spectra of CH_4 series prepared with and without the diamond barrier, the intensity of the defect related PL background is higher for the sample SEB2%+RR prepared with the diamond barrier and the diamond barrier thus seems to be worsening the $R_{SiV/bg}$. We would like to note that the sample SE2B% has the highest $R_{SiV/bg}$ from all the so far fabricated samples. In comparison with the sample SE2% fabricated within the CH_4 series, the $R_{SiV/bg}$ is better by the order of magnitude and we do not have the explanation for this difference so far. We were not able to reproduce such a good sample again using the same deposition parameters and thus this effect remains as one of the open questions that will be investigated in the near future.

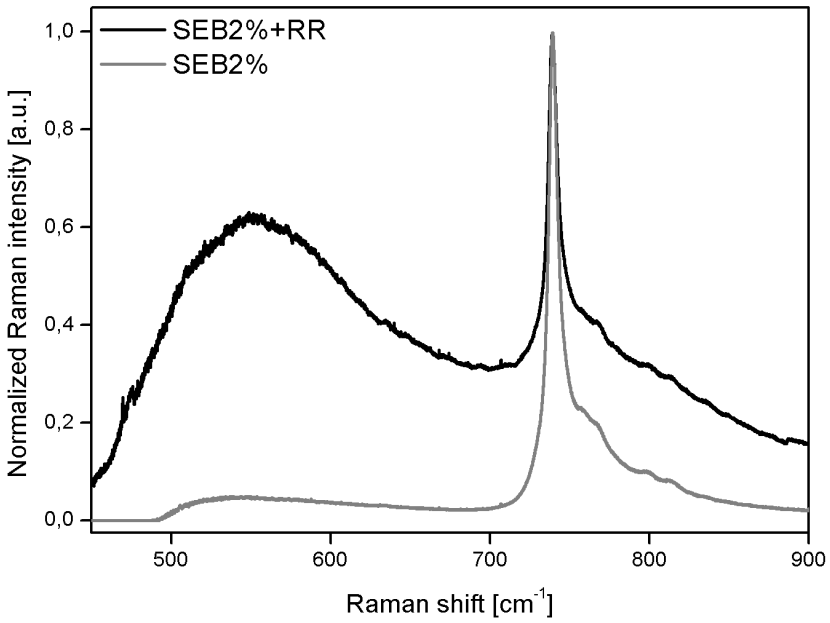

Figure 3.16: Normalized PL spectra of the samples SEB2% and SEB2%+RR.

3.5 Comparison of the diamond sample series

In this section, we would like to make comprehensive comparison between the samples grown with and without the protective diamond barrier and summarize results obtained by Raman and steady-state PL spectroscopy. Figure 3.17 shows Raman and PL spectra of the samples SE8%, SE8%+RR and SE15%+RR. We compare spectra of the samples SE8%, SE15%+RR because of having similar and almost similar Raman diamond peak positions to the monocrystalline reference, respectively, and in the same time having the highest SiV ZPL to the PL background ratio. The sample SE8%+RR was added to have direct comparison of samples grown with the same deposition parameters but differing in the starting material (glass for the SE8% and diamond barrier for the SE8%+RR). In Figure 3.17 a), we can see that the samples SE8%+RR and SE15%+RR grown with the protective diamond barrier posses strong TPA and G-band that are much higher in intensity than those of the sample SE8%. Unlike the samples SE8%, the Raman spectra of the samples SE8%+RR and SE15%+RR also show D-band. In Figure 3.17 b), we can see that the samples SE8%+RR and SE15%+RR grown with the protective diamond barrier possess higher PL background intensity with respect to the ZPL than the sample SE8%.

Figure 3.18 shows spectral peak positions of the Raman diamond peak and SiV ZPL obtained by fitting the Raman and PL spectra respectively with the Lorentz function 3.1. Figure 3.18 a) shows the obtained values of the Raman diamond peak spectral position. We can see that with increasing the amount of CH_4 in the atmosphere during the deposition, the Raman diamond spectral peak position of the samples grown with the protective diamond barrier increases towards the values of the monocrystalline diamond reference EDP. For the samples grown without the

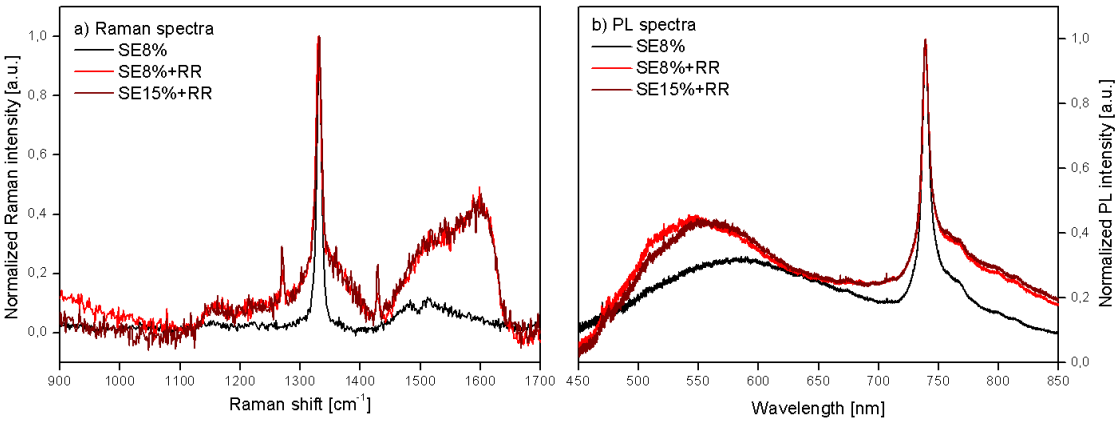

Figure 3.17: a) Raman spectra of the samples SE8%, SE8%+RR, and SE15%+RR normalized to the diamond peak. b) PL spectra of the samples SE8%, SE8%+RR, and SE15%+RR normalized to the SiV ZPL.

protective diamond barrier, we see that with increasing the amount of CH_4 in the atmosphere during growth the values of the spectral Raman diamond position slowly increase towards the monocrystalline reference sample EDP only for the samples SE2-8%. The samples SE6% and SE8% are the closest to the reference sample EDP in spectral peak position values. For the samples SE10-15%, the spectral peak position values exceed the value of the monocrystalline diamond reference EDP. Figure 3.18 b) shows the spectral peak positions of the SiV ZPL. We can see that with increasing the amount of CH_4 in the atmosphere during the deposition, the spectral position of the SiV ZPL decreases towards the monocrystalline diamond reference EDP for both series of samples, grown with or without the protective diamond barrier.

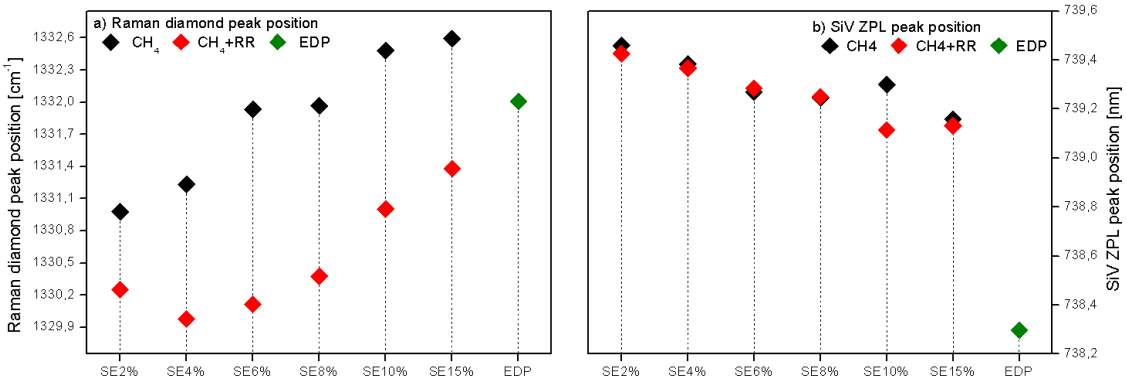

Figure 3.18: a) Spectral positions of the Raman diamond peak of the samples SE2-15%, SE2-15%+RR and EDP. b) Spectral position of the SiV ZPL of the samples SE2-15%, SE2-15%+RR and EDP.

Figure 3.19 shows comparison of the calculated values of $R_{SiV/bg}$ and DWF for the samples grown with and without the diamond barrier. We can see that the values

of both $R_{SiV/bg}$ and DWF are consistently lower for the samples grown with the diamond barrier than without, confirming that the diamond barrier seems to be worsening the optical properties of the prepared samples.

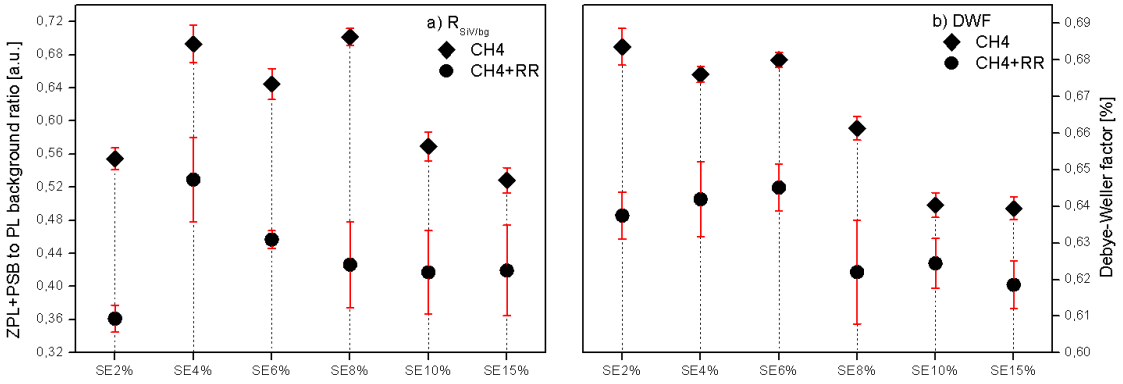

Figure 3.19: Calculated a) $R_{SiV/bg}$ and b) DWF values of the samples SE2-15% and SE2-15%+RR.

Figure 3.20 shows PL spectra of samples grown using 2% of CH_4, with and without diamond barrier, and with the SiH_4 gas flow switched off normalized to the defect-related PL background. We provide this PL spectra to further show that the diamond barrier is deterioating the $R_{SiV/bg}$. The high PL background at the spectral region of the SiV emission also does not enable to verify if the diamond barrier is serving its purpose which was to block the unwanted contamination of diamond with Si from the substrate. Based on the measured PL spectra we conclude that the diamond barrier is not needed to grow a sample with no SiV centers.

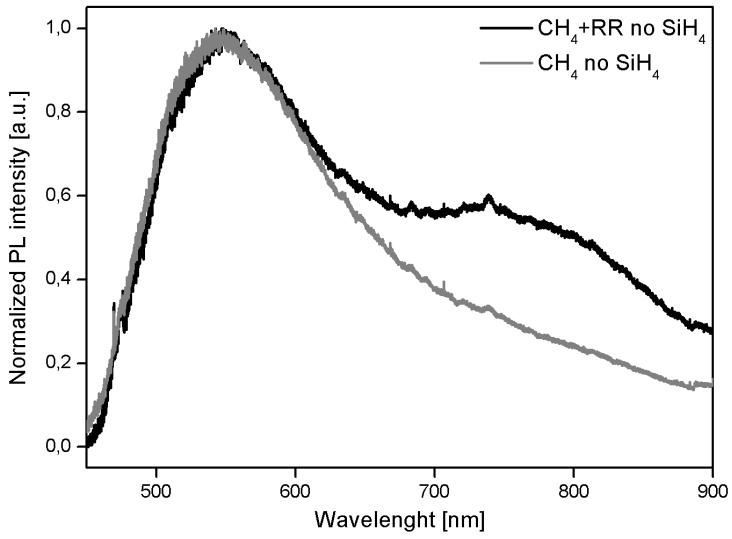

Figure 3.20: PL spectra of samples prepared using 2% of CH_4, with (black) and without (gray) diamond barrier, and with the SiH_4 gas flow switched off normalized to the PL background.

3.6 Time-resolved photoluminescence spectroscopy

Time-resolved PL spectra of the samples SE2-15% were measured in the spectral window of 565-820 nm and within the temporal window of 5 ns. The decay curves of the SiV ZPL were obtained by integrating the signal within 2 nm wide vertical window centered at the SiV ZPL maximum. These decay curves contain information not only about the decay dynamics of the SiV centers, but also about the decay dynamics of other defects. An example of the PL signal from the streak camera with the depicted 2 nm wide integrating window is shown in Figure 3.21 a). To obtain the information about the respective PL decay times, the decay curves were fitted with the following function

$$\begin{aligned} y \sim y_0 + A_1 \cdot (1 + \mathrm{erf}\,(-(x - x_0)/t_1) \cdot \exp(-(x - x_0)/t_1)) \\ + A_2 \cdot (1 + \mathrm{erf}\,(-(x - x_0)/t_2) \cdot \exp(-(x - x_0)/t_2)), \end{aligned} \tag{3.6}$$

where $A_{1,2}$ is an amplitude, x and y are independent variables and t_1 and t_2 are the decay times of the defects and the SiV centers respectively. An example of a decay curve fitted with the function 3.6 is shown in Figure 3.21 b).

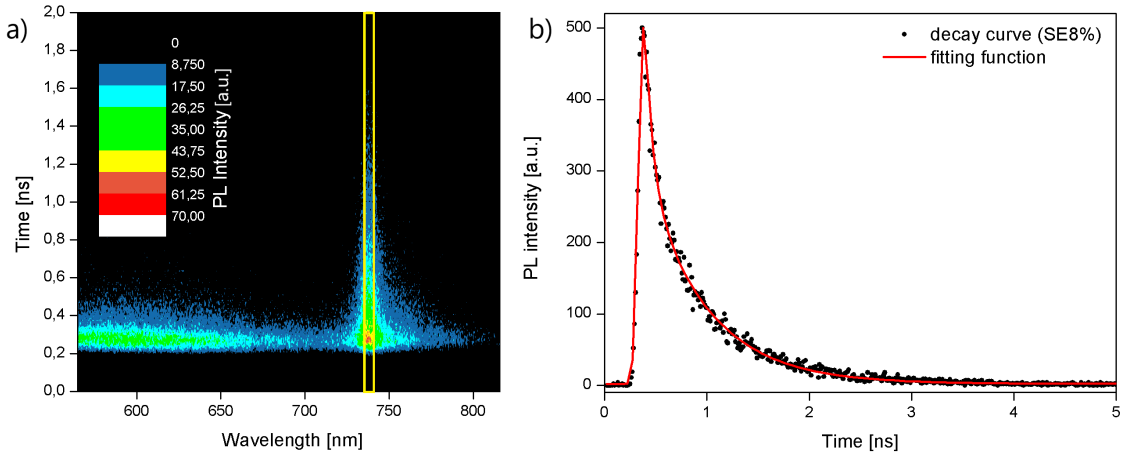

Figure 3.21: a) PL intensity of the sample SE8% as a function of the wavelength and time as measured by the streak camera. The integrating 2 ns spectral window used to obtain decay curves is depicted by yellow rectangle. b) Decay curve fitted with the function 3.6.

The obtained decay times are shown in Figure 3.22. We can see that with increasing the amount of CH_4 in the atmosphere during growth, the SiV ZPL decay times get shorter, but the defect-related PL decay times remain the same within the error margin. Along with the Raman spectra, the decrease in the SiV centers decay times with increasing the amount of CH_4 might be related to the coupling of the SiV centers ZPL to non-radiative defects. These defects are situated within the grains or at the surface as the propagation of the excited carriers from the SiVs to the sp^2 phase being in-between the grains is of low probability.

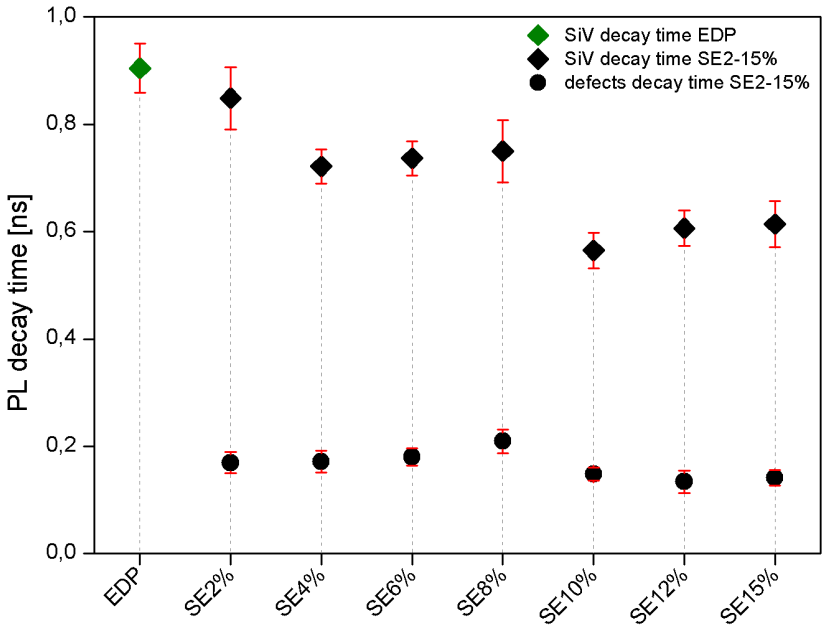

Figure 3.22: PL decay times of SiV ZPL and defects obtained by fitting the decay curves with the function 3.6.

3.7 Low temperature time-resolved photoluminescence spectroscopy.

Low temperature time-resolved PL spectra of the sample NCD were measured in the spectral window of 395-900 nm and within the temporal window of 10 ns. The decay curves of the SiV ZPL were obtained by integrating the signal within 2 nm wide vertical window centered at the SiV ZPL maximum. The defect decay curves were obtained by integrating the signal within 20 nm wide vertical window ranging from 640-660 nm. Figure 3.23 a) shows the SiV ZPL decay curves measured at the following temperatures: 12 K, 100 K, 200 K, 300 K and Figure 3.23 b) compares SiV ZPL and defect decay curves measured at 12 K.

To obtain the information about the dependence of the PL decay time on temperature, we fitted the decay curves in Origin with the function 3.6. Figure 3.24 a) shows the SiV ZPL decay times obtained for three different combinations of fitting parameters:
I) $A_1 = 0$, g as a free parameter – in this fit, the decay of the fast defects is not fitted directly ($A_1 = 0$) but included in the width g of the function describing the resolution of the detector.
II) $A_1 = 0$, $g = 0.19$ – in this fit, we fix the width g by the value evaluated from the response of the system to the short laser pulse and we assume that the decay of the fast defects is much shorter than this resolution hence it is omitted.
III) free A_1, $g = 0.19$ – here we fix the resolution of the system and try to extract the value of t_1 by the deconvolution.

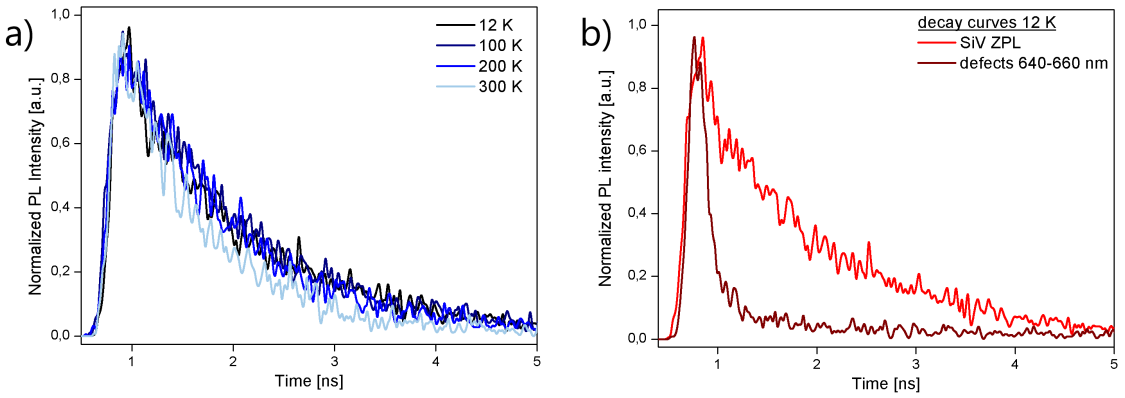

Figure 3.23: Low temperature decay curves. a) Normalized decay curves measured at 12 K, 100 K, 200 K and 300 K. b) Normalized SiV decay curves and defects (640-660 nm) decay curves measured at 12 K.

We tested these three combinations in order to evaluate the influence of uncertainty in the fit of the fast decay constant t_1 on the SiV ZPL decay times t_2. We can see that for all the three combinations of the fitting parameters, the SiV decay times get shorter with increasing temperature and that the results of the fits are at the given temperature for the most cases similar within the fitting error which evidences the correctness of the extracted t_2 value. The decrease of t_2 with increasing temperature suggests the existence of a non-radiative recombination channel at higher temperatures which was also observed in the previous section 3.6. The observed temperature dependence can be described by the Mott-Seitz model for the non-radiative relaxation in the following form

$$\tau = \tau_0/(1 + \alpha \exp(-\Delta E/k_B T)), \tag{3.7}$$

where τ and T are independent variables, τ_0 is the decay time, α is attempt frequency, ΔE is activation energy and k_B is the Boltzmann constant. The decay time τ_0 is the decay time at zero temperature. The obtained values of activation energy for the three cases are:

$$\begin{aligned} &A_1 \neq 0,\ g = 0.19 : \Delta E = 59,29307 \pm 16,44563 \text{ meV}, \\ &A_1 = 0,\ g \neq 0.19 : \Delta E = 57,97279 \pm 11,08706 \text{ meV}, \\ &A_1 = 0,\ g = 0.19 : \Delta E = 62,47685 \pm 12,35874 \text{ meV}. \end{aligned} \tag{3.8}$$

Figure 3.24 b) shows the defect-related decay times. By fitting the decay curves with the function 3.6, we obtained both fast and slow component of the defects decay. We can see that with increasing temperature, the decay times for the defects are also shortening.

Figure 3.25 shows low temperature time-resolved PL spectra. We can see that with decreasing the temperature, the intensity of the SiV ZPL peak increases. We can also see that upon cooling, the SiV ZPL spectral peak position shifts towards higher values. This so called blue shifting of the SiV ZPL upon cooling in accordance with literature. [28, 32, 33]

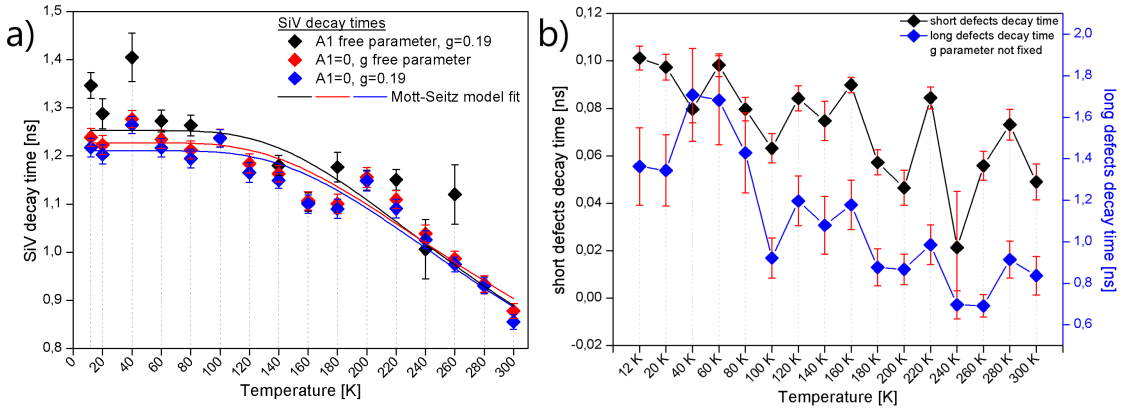

Figure 3.24: PL decay times as a function of the sample temperature. a) SiV center decay times obtained by fitting the decay curves with the function 3.6 using three different combinations of fitting parameters. The obtained decay times are further fitted with the Mott-Seitz model. b) Defect decay times obtained by fitting the decay curves with the function 3.6 without fixing the width parameter g.

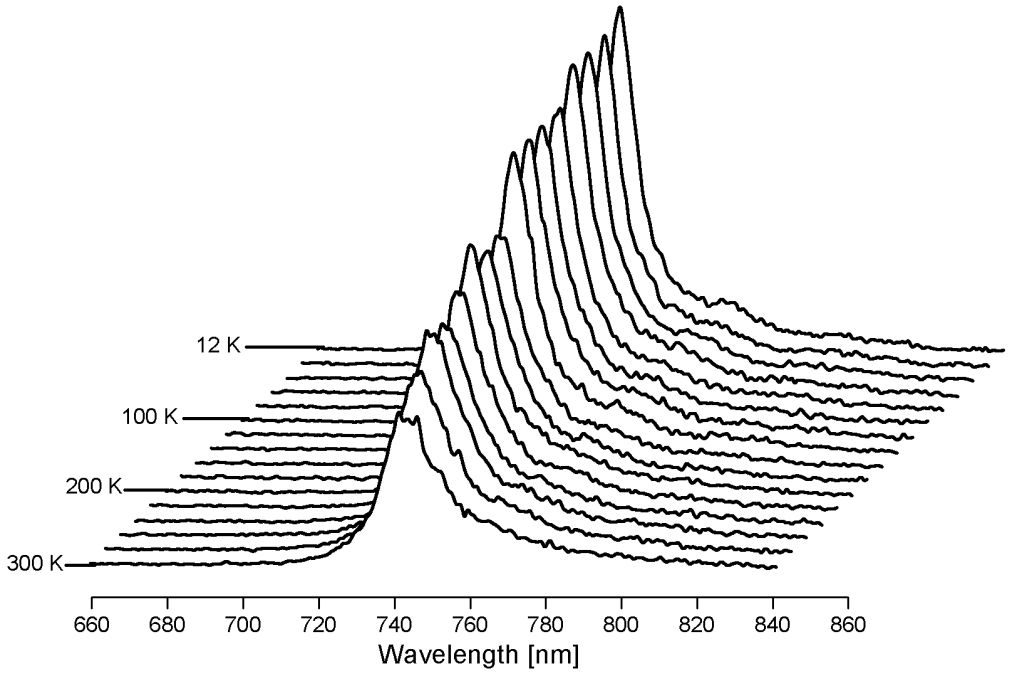

Figure 3.25: PL spectra of the sample NCD dependent on temperature.

To obtain more precise information about the values of the SiV ZPL spectral peak position and its dependence of temperature, we fitted only the SiV ZPL peak maximum in Origin with the Lorentz function 3.1. We also fitted the overall shape of the PL spectra in MATLAB using the combination of Lorentz and Gaussian functions in order to extract also the linewidth of the ZPL. The obtained SiV ZPL spectral peak positions are shown in Figure 3.26. The slight difference in the peak values of the two fits is arising from the uncertainty in the Matlab fit. We can see that the

SiV ZPL peak positions remains relatively constant for the temperatures 12-140 K and the blue shift starts around 160 K. From 160 K, the SiV ZPL peak position shifts rapidly. In order to fit the measured ZPL peak shift with a physical model, the obtained ZPL peak values were converted from nanometers to reciprocal centimeters and then the shift of the SiV ZPL maximum measured at 20-300 K with respect to the 12 K was calculated. The proposed temperature dependence models in literature are T^4 and aT^2+bT^4 where a, b are constants. [28, 35] The fit of the calculated data with these two functions is shown in Figure 3.26 b). We came to the same conclusion as in [28] and report that the the aT^2+bT^4 dependence fits our results more closely.

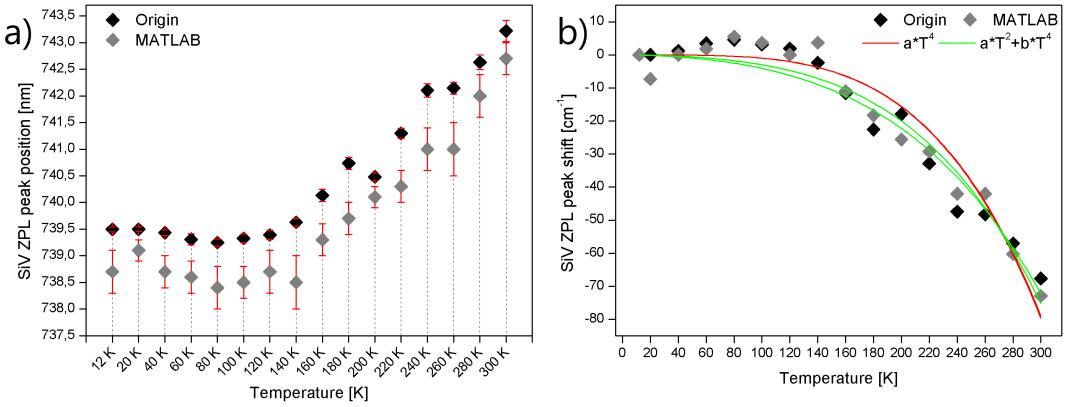

Figure 3.26: a) SiV ZPL peak position as a function of temperature. b) SiV ZPL shift as a function of temperature.

Figure 3.27 b) shows the temperature dependent values of the SiV ZPL width obtained by the MATLAB fit shown in Figure 3.27 a). We can see that with incereasing the remperature, the SiV ZPL width values are also increasing. We can see that from 12 K to 300 K, the SiV ZPL width value doubles. The temperature dependent broadening of the SiV ZPL is the result of electon-phonon coupling. [28]

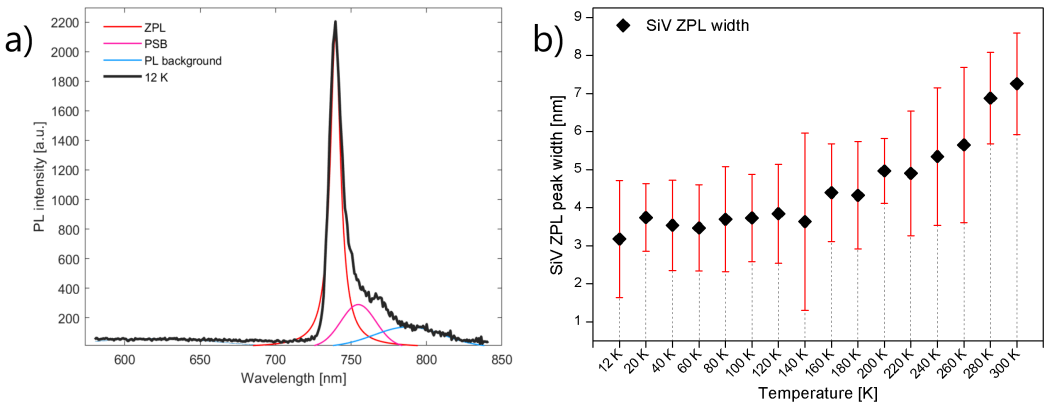

Figure 3.27: a) MATLAB fit of PL spectra measured at 12 K. b) Dependence of the width of the SiV ZPL on temperature.

Chapter 4

Conclusions

In this work, we prepared diamond thin films on quartz containing SiV centers by PE CVD. During the deposition, we systematically increased the amount of CH_4 to H_2 from 2 to 15%. Furthemore, we prepared samples with diamond barrier with the intention to prevent the sample contamination with the Si atoms from the SiO_2 substrate during the deposition. To investigate the structural changes, we employed the tools of Raman spectroscopy, SEM and AFM. To investigate the optical properties, we employed the tools of steady state and time-resolved PL spectroscopy. To investigate the temperature dependence of the SiV ZPL spectral position and PL decay times, we prepared the sample NCD and employed tools of low temperature time-resolved PL spectroscopy.

The Raman spectra showed that with increasing the amount of CH_4, the Raman diamond peak position of the samples SE2-8% slowly increases towards the monocrystalline reference sample EDP. The samples SE6% and SE8% matched the diamond Raman peak of the monocrystalline reference. For the samples SE10-15%, the diamond Raman peak position exceeded the value of the monocrystalline reference. The amount of TPA present in the samples also steadily increased as it was shown by the rise in the TPA peak situated around 1500 cm^{-1} and decrease in sp^3/TPA values. SEM images showed that with increasing the amount of CH_4, the individual diamond grains forming the polycrystalline diamond get smaller, increasing the overall surface area, and the surface of the samples seems to be closing in. This is in accordance with the Raman spectra and the rise in the amount of TPA. The TPA chains are situated at the grain boundaries and thus the increase in overall surface area leads to increase in the amount of TPA. AFM measurement showed that with increasing the amount of CH_4, the RMS values decrease, which is in accordance with the SEM images, and confirms that the surface of the samples is evening out.

The steady-state PL spectra showed that with increasing the amount of CH_4 present in the atmosphere during growth, the values of the SiV ZPL spectral position slowly decrease towards the monocrystalline reference sample EDP, which shows that with increasing the amount of CH_4 present in the atmosphere during growth the quality of the fabricated polycrystalline diamond is improving towards the monocrystalline diamond. We further processed the PL spectra and calculated the $R_{SiV/bg}$ and DWF. The samples with the highest values of $R_{SiV/bg}$ were the samples SE4-8%. All of the

calculated DWF values were between 64-69% which is in accordance with literature.

Both Raman and steady-state PL spectroscopy showed that the diamond barrier is worsening the properties of the prepared samples. Raman spectra showed that the presence of the diamond barrier results in increase in the content of sp^2 phase and steady state PL spectroscopy showed increase in the intensity of the defect-related PL background. The diamond barrier did not prevent the contamination of diamond with Si atoms from the substrate, however, its advantage might be that it presents a well-defined starting point of the deposition process.

Time-resolved PL spectroscopy gave us information about the decay dynamics of the SiV centers and the defects. With increasing the amount of CH_4 in the atmosphere during growth, the SiV ZPL PL decay times get shorter, but the defect-related PL decay times remain the same within the error margin. The decrease of the SiV centers decay times with increasing the amount of CH_4 was related to the coupling of the SiV centers ZPL emission to non-radiative defects.

Low temperature time-resolved PL spectroscopy measured for the sample NCD gave us insight into the temperature dependence of the peak position, decay time, and width of the SiV ZPL. In accordance with literature, we observed blue shift of the SiV ZPL spectral peak position. By calculating the SiV ZPL shift in repiprocal centimeters and fitting the data, we obtained aT^2+bT^4 dependence of the SiV ZPL peak position on temperature. We also observed widening of the SiV ZPL with increasing temperature. The SiV ZPL width values doubled when increasing the temperature from 12 to 300 K. Furthemore, we observed shortening of the SiV PL decay times at higher temperatures suggesting the existence of a non-radiative recombination channel as previously mentioned.

One of the goals of this study was to optimize deposition parameters to suppress PL background and thus to prepare samples suitable for applications in optics and bio-sensing. We conclude that the samples SE4-8% present the best candidates for applications where the low content of non-radiative defects and high $R_{SiV/bg}$ are necessary.

Bibliography

[1] A. M. Zaitsev, *Optical properties of diamond: A Data Handbook*. Springer, 2001.

[2] C. Wild, N. Herres, and P. Koidl, "Texture formation in polycrystalline diamond films," *Journal of Applied Physics*, vol. 68, no. 3, pp. 973–978, 1990.

[3] S. Lagomarsino, A. M. Flatae, H. Kambalathmana, F. Sledz, L. Hunold, N. Soltani, P. Reuschel, S. Sciortino, N. Gelli, M. Massi, C. Czelusniak, L. Giuntini, and M. Agio, "Creation of silicon-vacancy color centers in diamond by ion implantation," *Frontiers in Physics*, vol. 8, 2021.

[4] J. M. Smith, S. A. Meynell, A. C. B. Jayich, and J. Meijer, "Colour centre generation in diamond for quantum technologies," *Nanophotonics*, vol. 8, no. 11, pp. 1889–1906, 2019.

[5] L. Rayleigh, "XXXIV. On the transmission of light through an atmosphere containing small particles in suspension, and on the origin of the blue of the sky," *Applied Optics*, vol. 47, no. 287, pp. 375–384, 1899.

[6] A. T. Young, "Rayleigh scattering," *Applied Optics*, vol. 20, no. 4, pp. 533–535, 1981.

[7] G. Mie, "Beiträge zur optik trüber medien, speziell kolloidaler metallösungen (contributions to the optics of turbid media, particularly solutions of colloidal metals)," *Annalen der Physik*, vol. 330, no. 3, pp. 377–445, 1908.

[8] "Thermofischer Scientific website (`https://www.thermofisher.com/blog/materials/sem-signal-types-electrons-and-the-information-they-provide`)."

[9] "JPK Instruments Nanowizard AFM Handbook (`https://www.nanophys.kth.se/nanolab/afm/jpk/manuf-manuals/handbook-2.2a.pdf`)."

[10] I. Pelant and J. Valenta, *Luminescence spectroscopy of semiconductors*. Oxford University Press, 2016.

[11] I. Pelant and J. Valenta, *Luminiscenční spektroskopie I: Objemové krystalické polovodiče*. Academia, 2006.

[12] "Hamamatsu Photonics Universal streak camera catalogue (`https://www.hamamatsu.com/content/dam/hamamatsu-photonics/sites/documents/99_SALES_LIBRARY/sys/SHSS0016E_C10910s.pdf`)."

[13] R. More and J. Bokros, *Biomaterials: Carbon.* Oxford University Press, 2006.

[14] W. Saslow, T. K. Bergstresser, and M. L. Cohen, "Band structure and optical properties of diamond," *Physical Review Letters*, vol. 16, pp. 354–356, 1966.

[15] G. Davies and M. F. Hamer, "Optical studies of the 1.945 ev vibronic band in diamond," *Proceedings of the Royal Society A*, vol. 348, pp. 285–298, 1976.

[16] A. Gali, "Ab initio theory of the nitrogen-vacancy center in diamond," *Nanophotonics*, vol. 8, no. 11, pp. 1907–1943, 2019.

[17] M. W. Doherty, N. B. Manson, P. Delaney, and L. C. L. Hollenberg, "The negatively charged nitrogen-vacancy centre in diamond: the electronic solution," *Nanophotonics*, vol. 13, no. 2, p. 025019, 2011.

[18] H.-Q. Zhao, M. Fujiwara, and S. Takeuchi, "Suppression of fluorescence phonon sideband from nitrogen vacancy centers in diamond nanocrystals by substrate effect," *Optics Express*, vol. 20, no. 14, pp. 15628–15635, 2012.

[19] S. Karaveli, O. Gaathon, A. Wolcott, R. Sakakibara, O. A. Shemesh, D. S. Peterka, E. S. Boyden, J. S. Owen, R. Yuste, and D. Englund, "Modulation of nitrogen vacancy charge state and fluorescence in nanodiamonds using electrochemical potential," *Optics Express*, vol. 113, no. 15, pp. 3938–3943, 2016.

[20] C. Bradac, W. Gao, J. Forneris, M. E. Trusheim, and I. Aharonovich, "Quantum nanophotonics with group iv defects in diamond," *Nature Communications*, vol. 10, 2019.

[21] E. Neu, D. Steinmetz, J. Riedrich-Möller, S. Gsell, M. Fischer, M. Schreck, and C. Becher, "Single photon emission from silicon-vacancy colour centres in chemical vapour deposition nano-diamonds on iridium," *New Journal of Physics*, vol. 13, no. 2, p. 025012, 2011.

[22] E. Neu, M. Fischer, S. Gsell, M. Schreck, and C. Becher, "Fluorescence and polarization spectroscopy of single silicon vacancy centers in heteroepitaxial nanodiamonds on iridium," *Physical Review B*, vol. 84, p. 205211, 2011.

[23] S. Häußler, G. Thiering, A. Dietrich, N. Waasem, T. Teraji, J. Isoya, T. Iwasaki, M. Hatano, F. Jelezko, A. Gali, and A. Kubanek, "Photoluminescence excitation spectroscopy of siv and gev color center in diamond," *New Journal of Physics*, vol. 19, no. 6, p. 063036, 2017.

[24] L. J. Rogers, K. D. Jahnke, M. W. Doherty, A. Dietrich, L. P. McGuinness, C. Müller, T. Teraji, H. Sumiya, J. Isoya, N. B. Manson, and F. Jelezko, "Electronic structure of the negatively charged silicon-vacancy center in diamond," *Physical Review B*, vol. 89, p. 235101, 2014.

[25] C. Hepp, T. Müller, V. Waselowski, J. N. Becker, B. Pingault, H. Sternschulte, D. Steinmüller-Nethl, A. Gali, J. R. Maze, M. Atatüre, and C. Becher, "Electronic structure of the silicon vacancy color center in diamond," *Physical Review Letters*, vol. 112, p. 036405, 2014.

[26] Y. Zhou, A. Rasmita, K. Li, Q. Xiong, I. Aharonovich, and W. Gao, "Coherent control of a strongly driven silicon vacancy optical transition in diamond," *Nature Communications*, vol. 8, 2017.

[27] S. M. Barnett and P. M. Radmore, *Methods in Theoretical Quantum Optics*. Clarendon Press, 1997.

[28] E. Neu, C. Hepp, M. Hauschild, S. Gsell, M. Fischer, H. Sternschulte, D. Steinmüller-Neth, M. Schreck, and C. Becher, "Low-temperature investigations of single silicon vacancy colour centres in diamond," *New Journal of Physics*, vol. 15, no. 4, p. 043005, 2013.

[29] A. Razgulov, S. Lyapin, A. Novikov, and E. Ekimov, "Low-temperature photoluminescence study of snv centers in hpht diamond," *Diamond and Related Materials*, vol. 116, p. 108379, 2021.

[30] L. J. Rogers, K. D. Jahnke, M. H. Metsch, A. Sipahigil, J. M. Binder, T. Teraji, H. Sumiya, J. Isoya, M. D. Lukin, P. Hemmer, and F. Jelezko, "All-optical initialization, readout, and coherent preparation of single silicon-vacancy spins in diamond," *Physical Review Letters*, vol. 113, p. 263602, 2014.

[31] B. Pingault, J. N. Becker, C. H. Schulte, C. Arend, C. Hepp, T. Godde, A. I. Tartakovskii, M. Markham, C. Becher, and M. Atatüre, "All-optical formation of coherent dark states of silicon-vacancy spins in diamond," *Physical Review Letters*, vol. 113, p. 263601, 2014.

[32] A. A. Gorokhovsky, A. V. Turukhin, and R. R. Alfano, "Photoluminescence vibrational structure of si center in chemical-vapor deposited diamond," *Applied Physics Letters*, vol. 66, no. 1, pp. 43–45, 1995.

[33] T. Feng and B. D. Schwartz, "Characteristics and origin of the 1.681 ev luminescence center in chemical-vapordeposited diamond films," *Journal of Applied Physics*, vol. 73, no. 3, pp. 1415–1425, 1993.

[34] G. Davies, "Vibronic spectra in diamond," *Journal of Physics C: Solid State Physics*, vol. 7, no. 20, p. 3797, 1974.

[35] V. Hizhnyakov, H. Kaasik, and I. Sildos, "Zero-phonon lines: The effect of a strong softening of elastic springs in the excited state," *Physica Status Solidi (B)*, vol. 234, no. 2, pp. 644–653, 2002.

[36] Y. Varshni, "Temperature dependence of the energy gap in semiconductors," *Physica*, vol. 34, no. 1, pp. 149–154, 1967.

[37] O. A. Williams and M. Nesládek, "Growth and properties of nanocrystalline diamond films," *Physica status solidi (a)*, vol. 203, no. 13, pp. 3375–3386, 2006.

[38] W. G. S. Leigh, E. L. H. Thomas, J. A. Cuenca, S. Mandal, and O. A. Williams, "In-situ monitoring of microwave plasma-enhanced chemical vapour deposition diamond growth on silicon using spectroscopic ellipsometry," *Carbon*, vol. 202, pp. 204–212, 2023.

[39] A. Gicquel, K. Hassouni, F. Silva, and J. Achard, "Cvd diamond films: from growth to applications," *Current Applied Physics*, vol. 1, no. 6, pp. 479–496, 2001.

[40] S. Potocky, A. Kromka, J. Potmesil, Z. Remes, V. Vorlicek, M. Vanecek, and M. Michalka, "Investigation of nanocrystalline diamond films grown on silicon and glass at substrate temperature below 400°c," *Diamond and Related Materials*, vol. 16, no. 4, pp. 744–747, 2007.

[41] S. Potocky, A. Kromka, J. Potmesil, Z. Remes, Z. Polackova, and M. Vanecek, "Growth of nanocrystalline diamond films deposited by microwave plasma cvd system at low substrate temperatures," *physica status solidi (a)*, vol. 203, no. 12, pp. 3011–3015, 2006.

[42] C. Blin, X. Checoury, H. A. Girard, C. Gesset, S. Saada, P. Boucaud, and P. Bergonzo, "Optical analysis of p-type surface conductivity in diamond with slotted photonic crystals," *Advanced Optical Materials*, vol. 1, no. 12, pp. 963–970, 2013.

[43] L. Ondič, K. Dohnalová, M. Ledinský, A. Kromka, O. Babchenko, and B. Rezek, "Effective extraction of photoluminescence from a diamond layer with a photonic crystal," *ACS Nano*, vol. 5, pp. 346–350, 2011.

[44] G. Pitruzzello and T. F. Krauss, "Photonic crystal resonances for sensing and imaging," *Journal of Optics*, vol. 20, no. 7, p. 073004, 2018.

[45] S. T. Lee, Z. Lin, and X. Jiang, "Cvd diamond films: nucleation and growth," *Materials Science and Engineering: R: Reports*, vol. 25, no. 4, pp. 123–154, 1999.

[46] J. Isberg, J. Hammersberg, E. Johansson, T. Wikström, D. J. Twitchen, A. J. Whitehead, S. E. Coe, and G. A. Scarsbrook, "High carrier mobility in single-crystal plasma-deposited diamond," *Science*, vol. 297, no. 5587, pp. 1670–1672, 2002.

[47] N. Felgen, A. Schmidt, B. Naydenov, F. Jelezko, J. P. Reithmaier, and C. Popov, *Quantum Information Technology and Sensing Based on Color Centers in Diamond*, pp. 193–214. Springer Netherlands, 2018.

[48] A. Faraon, C. Santori, Z. Huang, K. M. C. Fu, V. M. Acosta, D. Fattal, and R. G. Beausoleil, "Quantum photonic devices in single-crystal diamond," *New Journal of Physics*, vol. 15, no. 2, p. 025010, 2013.

[49] D. Nečas and P. Klapetek, "Gwyddion: an open-source software for spm data analysis," *Central European Journal of Physics.*, vol. 10, no. 1, pp. 181–188, 2012.

[50] A. Dychalska, P. Popielarski, W. Franków, K. Fabisiak, K. Paprocki, and M. Szybowicz, "Study of cvd diamond layers with amorphous carbon admixture by raman scattering spectroscopy," *Materials Science-Poland*, vol. 33, pp. 799–805, 2015.

[51] V. I. Korepanov, H. Hamaguchi, E. Osawa, V. Ermolenkov, I. K. Lednev, B. J. M. Etzold, O. Levinson, B. Zousman, C. P. Epperla, and H. Chang, "Carbon structure in nanodiamonds elucidated from raman spectroscopy," *Carbon*, vol. 121, pp. 322–329, 2017.

[52] F. B. Schügerl and H. Kuzmany, "Optical modes of trans-polyacetylene," *Journal of Chemical Physics*, vol. 74, no. 2, pp. 953–958, 1981.

[53] T. López-Ríos, Sandré, S. Leclercq, and Sauvain, "Polyacetylene in diamond films evidenced by surface enhanced raman scattering," *Physical Review Letters*, vol. 76, pp. 4935–4938, 1996.

[54] R. Pfeiffer, H. Kuzmany, P. Knoll, S. Bokova, N. Salk, and B. Günther, "Evidence for trans-polyacetylene in nano-crystalline diamond films," *Diamond and Related Materials*, vol. 12, no. 3, pp. 268–271, 2003.

[55] "OriginPro, Version 8. OriginLab Corporation, Northampton, MA, USA."

[56] W. Fortunato, A. J. Chiquito, J. C. Galzerani, and J. R. Moro, "Crystalline quality and phase purity of cvd diamond films studied by raman spectroscopy," *Journal of Materials Science*, vol. 42, pp. 7331–7336, 2007.

[57] P. Galář, B. Dzurňák, M. Varga, M. Marton, A. Kromka, and P. Malý, "Influence of non-diamond carbon phase on recombination mechanisms of photoexcited charge carriers in microcrystalline and nanocrystalline diamond studied by time resolved photoluminescence spectroscopy," *Journal of Materials Science*, vol. 4, no. 4, pp. 624–637, 2014.

[58] M. Malakoutian, M. A. Laurent, and S. Chowdhury, "A study on the growth window of polycrystalline diamond on si3n4-coated n-polar gan," *Crystals*, vol. 9, no. 10, 2019.